LARGE-SCALE DISTRIBUTION OF ARRIVAL DIRECTIONS OF COSMIC RAYS DETECTED ABOVE 10[18] eV AT THE PIERRE AUGER OBSERVATORY

The Pierre Auger Collaboration[1]

P. Abreu[2], M. Aglietta[3], M. Ahlers[4], E. J. Ahn[5], I. F. M. Albuquerque[6], D. Allard[7], I. Allekotte[8], J. Allen[9], P. Allison[10], A. Almela[11,12], J. Alvarez Castillo[13], J. Alvarez-Muñiz[14], R. Alves Batista[15], M. Ambrosio[16], A. Aminaei[17], L. Anchordoqui[18], S. Andringa[2], T. Antiči'c[19], C. Aramo[16], E. Arganda[20,21], F. Arqueros[21], H. Asorey[8], P. Assis[2], J. Aublin[22], M. Ave[23], M. Avenier[24], G. Avila[25], A. M. Badescu[26], M. Balzer[27], K. B. Barber[28], A. F. Barbosa[29,96], R. Bardenet[30], S. L. C. Barroso[31], B. Baughman[10,97], J. Bäuml[32], C. Baus[23], J. J. Beatty[10], K. H. Becker[33], A. Bellétoile[34], J. A. Bellido[28], S. BenZvi[4], C. Berat[24], X. Bertou[8], P. L. Biermann[35], P. Billoir[22], F. Blanco[21], M. Blanco[22,36], C. Bleve[33], H. Blümer[23,32], M. Boháčová[37], D. Boncioli[38], C. Bonifazi[22,39], R. Bonino[3], N. Borodai[40], J. Brack[41], I. Brancus[42], P. Brogueira[2], W. C. Brown[43], R. Bruijn[44,98], P. Buchholz[45], A. Bueno[46], L. Buroker[18], R. E. Burton[47], K. S. Caballero-Mora[48], B. Caccianiga[49], L. Caramete[35], R. Caruso[50], A. Castellina[3], O. Catalano[51], G. Cataldi[52], L. Cazon[2], R. Cester[53], J. Chauvin[24], S. H. Cheng[48], A. Chiavassa[3], J. A. Chinellato[15], J. Chirinos Diaz[54], J. Chudoba[37], M. Cilmo[16], R. W. Clay[28], G. Cocciolo[52], L. Collica[49], M. R. Coluccia[52], R. Conceição[2], F. Contreras[55], H. Cook[44], M. J. Cooper[28], J. Coppens[17,56], A. Cordier[30], S. Coutu[48], C. E. Covault[47], A. Creusot[7], A. Criss[48], J. Cronin[57], A. Curutiu[35], S. Dagoret-Campagne[30], R. Dallier[34], B. Daniel[15], S. Dasso[58,59], K. Daumiller[32], B. R. Dawson[28], R. M. de Almeida[60], M. De Domenico[50], C. De Donato[13], S. J. de Jong[17,56], G. De La Vega[61], W. J. M. de Mello Junior[15], J. R. T. de Mello Neto[39], I. De Mitri[52], V. de Souza[62], K. D. de Vries[63], L. del Peral[36], M. del Río[38,55], O. Deligny[64], H. Dembinski[23], N. Dhital[54], C. Di Giulio[38,65], M. L. Díaz Castro[29], P. N. Diep[66], F. Diogo[2], C. Dobrigkeit[15], W. Docters[63], J. C. D'Olivo[13], P. N. Dong[64,66], A. Dorofeev[41], J. C. dos Anjos[29], M. T. Dova[20], D. D'Urso[16], I. Dutan[35], J. Ebr[37], R. Engel[32], M. Erdmann[67], C. O. Escobar[5,15], J. Espadanal[2], A. Etchegoyen[11,12], P. Facal San Luis[57], H. Falcke[17,56,68], K. Fang[57], G. Farrar[9], A. C. Fauth[15], N. Fazzini[5], A. P. Ferguson[47], B. Fick[54], J. M. Figueira[12], A. Filevich[12], A. Filipčič[69,70], S. Fliescher[67], C. E. Fracchiolla[41], E. D. Fraenkel[63], O. Fratu[26], U. Fröhlich[45], B. Fuchs[23], R. Gaior[22], R. F. Gamarra[12], S. Gambetta[71], B. García[61], S. T. Garcia Roca[14], D. Garcia-Gamez[30], D. Garcia-Pinto[21], G. Garilli[50], A. Gascon Bravo[46], H. Gemmeke[27], P. L. Ghia[22], M. Giller[72], J. Gitto[61], H. Glass[5], M. S. Gold[73], G. Golup[8], F. Gomez Albarracin[20], M. Gómez Berisso[8], P. F. Gómez Vitale[25], P. Gonçalves[2], J. G. Gonzalez[32], B. Gookin[41], A. Gorgi[3], P. Gouffon[6], E. Grashorn[10], S. Grebe[17,56], N. Griffith[10], A. F. Grillo[74], Y. Guardincerri[59], F. Guarino[16], G. P. Guedes[75], P. Hansen[20], D. Harari[8], T. A. Harrison[28], J. L. Harton[41], A. Haungs[32], T. Hebbeker[67], D. Heck[32], A. E. Herve[28], G. C. Hill[28], C. Hojvat[5], N. Hollon[57], V. C. Holmes[28], P. Homola[40], J. R. Hörandel[17,56], P. Horvath[76], M. Hrabovský[37,76], D. Huber[23], T. Huege[32], A. Insolia[50], F. Ionita[57], A. Italiano[50], S. Jansen[17,56], C. Jarne[20], S. Jiraskova[17], M. Josebachuili[12], K. Kadija[19], K. H. Kampert[33], P. Karhan[77], P. Kasper[5], I. Katkov[23], B. Kégl[30], B. Keilhauer[32], A. Keivani[78], J. L. Kelley[17], E. Kemp[15], R. M. Kieckhafer[54], H. O. Klages[32], M. Kleifges[27], J. Kleinfeller[32,55], J. Knapp[44], D.-H. Koang[24], K. Kotera[57], N. Krohm[33], O. Krömer[27], D. Kruppke-Hansen[33], D. Kuempel[45,67], J. K. Kulbartz[79], N. Kunka[27], G. La Rosa[51], C. Lachaud[7], D. LaHurd[47], L. Latronico[3], R. Lauer[73], P. Lautridou[34], S. Le Coz[24], M. S. A. B. Leão[80], D. Lebrun[24], P. Lebrun[5], M. A. Leigui de Oliveira[80], A. Letessier-Selvon[22], I. Lhenry-Yvon[64], K. Link[23], R. López[81], A. Lopez Agüera[14], K. Louedec[24,30], J. Lozano Bahilo[46], L. Lu[44], A. Lucero[12], M. Ludwig[23], H. Lyberis[39,64], M. C. Maccarone[51], C. Macolino[22], S. Maldera[3], J. Maller[34], D. Mandat[37], P. Mantsch[5], A. G. Mariazzi[20], J. Marin[3,55], V. Marin[34], I. C. Maris[22], H. R. Marquez Falcon[82], G. Marsella[52], D. Martello[52], L. Martin[34], H. Martinez[83], O. Martínez Bravo[81], D. Martraire[64], J. J. Masías Meza[59], H. J. Mathes[32], J. Matthews[78], J. A. J. Matthews[73], G. Matthiae[38], D. Maurel[32], D. Maurizio[29,53], P. O. Mazur[5], G. Medina-Tanco[13], M. Melissas[23], D. Melo[12], E. Menichetti[53], A. Menshikov[27], P. Mertsch[84], S. Messina[63], C. Meurer[67], R. Meyhandan[85], S. Mi'canovi'c[19], M. I. Micheletti[86], I. A. Minaya[21], L. Miramonti[49], L. Molina-Bueno[46], S. Mollerach[8], M. Monasor[57], D. Monnier Ragaigne[30], F. Montanet[24], B. Morales[13], C. Morello[3], E. Moreno[81], J. C. Moreno[20], M. Mostafá[41], C. A. Moura[80], M. A. Muller[15], G. Müller[67], M. Münchmeyer[22], R. Mussa[53], G. Navarra[3,96], J. L. Navarro[46], S. Navas[46], P. Necesal[37], L. Nellen[13], A. Nelles[17,56], J. Neuser[33], P. T. Nhung[66], M. Niechciol[45], L. Niemietz[33], N. Nierstenhoefer[33], D. Nitz[54], D. Nosek[77], L. Nožka[37], J. Oehlschläger[32], A. Olinto[57], M. Ortiz[21], N. Pacheco[36], D. Pakk Selmi-Dei[15], M. Palatka[37], J. Pallotta[87], N. Palmieri[23], G. Parente[14], E. Parizot[7], A. Parra[14], S. Pastor[88], T. Paul[89], M. Pech[37], J. Pękala[40], R. Pelayo[14,81], I. M. Pepe[90], L. Perrone[52], R. Pesce[71], E. Petermann[91], S. Petrera[65], A. Petrolini[71], Y. Petrov[41], C. Pfendner[4], R. Piegaia[59], T. Pierog[32], P. Pieroni[59], M. Pimenta[2], V. Pirronello[50], M. Platino[12], M. Plum[67], V. H. Ponce[8], M. Pontz[45], A. Porcelli[32], P. Privitera[57], M. Prouza[37], E. J. Quel[87], S. Querchfeld[33], J. Rautenberg[33], O. Ravel[34], D. Ravignani[12], B. Revenu[34], J. Ridky[37], S. Riggi[14], M. Risse[45], P. Ristori[87], H. Rivera[49], V. Rizi[65], J. Roberts[9], W. Rodrigues de Carvalho[14], G. Rodriguez[14], I. Rodriguez Cabo[14], J. Rodriguez Martino[55], J. Rodriguez Rojo[55], M. D. Rodríguez-Frías[36], G. Ros[36], J. Rosado[21], T. Rossler[76], M. Roth[32], B. Rouillé-d'Orfeuil[57], E. Roulet[8], A. C. Rovero[58], C. Rühle[27], A. Saftoiu[42], F. Salamida[64], H. Salazar[81], F. Salesa Greus[41], G. Salina[38], F. Sánchez[12],

C. E. Santo[2], E. Santos[2], E. M. Santos[39], F. Sarazin[92], B. Sarkar[33], S. Sarkar[84], R. Sato[55], N. Scharf[67], V. Scherini[49], H. Schieler[32], P. Schiffer[67,79], A. Schmidt[27], O. Scholten[63], H. Schoorlemmer[17,56], J. Schovancova[37], P. Schovánek[37], F. Schröder[32], D. Schuster[92], S. J. Sciutto[20], M. Scuderi[50], A. Segreto[51], M. Settimo[45], A. Shadkam[78], R. C. Shellard[29], I. Sidelnik[12], G. Sigl[79], H. H. Silva Lopez[13], O. Sima[93], A. 'Smiałkowski[72], R. Šmída[32], G. R. Snow[91], P. Sommers[48], J. Sorokin[28], H. Spinka[5,94], R. Squartini[55], Y. N. Srivastava[89], S. Stanic[70], J. Stapleton[10], J. Stasielak[40], M. Stephan[67], A. Stutz[24], F. Suarez[12], T. Suomijärvi[64], A. D. Supanitsky[58], T. Šuša[19], M. S. Sutherland[78], J. Swain[89], Z. Szadkowski[72], M. Szuba[32], A. Tapia[12], M. Tartare[24], O. Taşcău[33], R. Tcaciuc[45], N. T. Thao[66], D. Thomas[41], J. Tiffenberg[59], C. Timmermans[17,56], W. Tkaczyk[72,96], C. J. Todero Peixoto[62], G. Toma[42], L. Tomankova[37], B. Tomé[2], A. Tonachini[53], G. Torralba Elipe[14], P. Travnicek[37], D. B. Tridapalli[6], G. Tristram[7], E. Trovato[50], M. Tueros[14], R. Ulrich[32], M. Unger[32], M. Urban[30], J. F. Valdés Galicia[13], I. Valiño[14], L. Valore[16], G. van Aar[17], A. M. van den Berg[63], S. van Velzen[17], A. van Vliet[79], E. Varela[81], B. Vargas Cárdenas[13], J. R. Vázquez[21], R. A. Vázquez[14], D. Veberič[69,70], V. Verzi[38], J. Vicha[37], M. Videla[61], L. Villaseñor[82], H. Wahlberg[20], P. Wahrlich[28], O. Wainberg[11,12], D. Walz[67], A. A. Watson[44], M. Weber[27], K. Weidenhaupt[67], A. Weindl[32], F. Werner[32], S. Westerhoff[4], B. J. Whelan[28,48], A. Widom[89], G. Wieczorek[72], L. Wiencke[92], B. Wilczyńska[40], H. Wilczyński[40], M. Will[32], C. Williams[57], T. Winchen[67], M. Wommer[32], B. Wundheiler[12], T. Yamamoto[57,99], T. Yapici[54], P. Younk[45,95], G. Yuan[78], A. Yushkov[14], B. Zamorano Garcia[46], E. Zas[14], D. Zavrtanik[69,70], M. Zavrtanik[69,70], I. Zaw[9,100], A. Zepeda[83,101], J. Zhou[57], Y. Zhu[27], M. Zimbres Silva[15,33], AND M. Ziolkowski[45]

[1] Av. San Martín Norte 306, 5613 Malargüe, Mendoza, Argentina; www.auger.org
[2] LIP and Instituto Superior Técnico, Technical University of Lisbon, Portugal
[3] Istituto di Fisica dello Spazio Interplanetario (INAF), Università di Torino and Sezione INFN, Torino, Italy
[4] University of Wisconsin, Madison, WI, USA
[5] Fermilab, Batavia, IL, USA
[6] Instituto de Física, Universidade de São Paulo, São Paulo, SP, Brazil
[7] Laboratoire AstroParticule et Cosmologie (APC), Université Paris 7, CNRS-IN2P3, Paris, France
[8] Centro Atómico Bariloche and Instituto Balseiro (CNEA-UNCuyo-CONICET), San Carlos de Bariloche, Argentina
[9] New York University, New York, NY, USA
[10] Ohio State University, Columbus, OH, USA
[11] Facultad Regional Buenos Aires, Universidad Tecnológica Nacional, Buenos Aires, Argentina
[12] Instituto de Tecnologías en Detección y Astropartículas (CNEA, CONICET, UNSAM), Buenos Aires, Argentina
[13] Universidad Nacional Autonoma de Mexico, Mexico, D. F., Mexico
[14] Universidad de Santiago de Compostela, Spain
[15] IFGW, Universidade Estadual de Campinas, Campinas, SP, Brazil
[16] Università di Napoli "Federico II" and Sezione INFN, Napoli, Italy
[17] IMAPP, Radboud University Nijmegen, The Netherlands
[18] University of Wisconsin, Milwaukee, WI, USA
[19] Rudjer Boškovi'c Institute, 10000 Zagreb, Croatia
[20] IFLP, Universidad Nacional de La Plata and CONICET, La Plata, Argentina
[21] Universidad Complutense de Madrid, Madrid, Spain
[22] Laboratoire de Physique Nucléaire et de Hautes Energies (LPNHE), Universités Paris 6 et Paris 7, CNRS-IN2P3, Paris, France
[23] Karlsruhe Institute of Technology-Campus South-Institut für Experimentelle Kernphysik (IEKP), Karlsruhe, Germany
[24] Laboratoire de Physique Subatomique et de Cosmologie (LPSC), Université Joseph Fourier Grenoble, CNRS-IN2P3, Grenoble INP, France
[25] Observatorio Pierre Auger and Comisión Nacional de Energía Atómica, Malargüe, Argentina
[26] University Politehnica of Bucharest, Romania
[27] Karlsruhe Institute of Technology-Campus North-Institut für Prozessdatenverarbeitung und Elektronik, Karlsruhe, Germany
[28] University of Adelaide, Adelaide, SA, Australia
[29] Centro Brasileiro de Pesquisas Fisicas, Rio de Janeiro, RJ, Brazil
[30] Laboratoire de l'Accélérateur Linéaire (LAL), Université Paris 11, CNRS-IN2P3, France
[31] Universidade Estadual do Sudoeste da Bahia, Vitoria da Conquista, BA, Brazil
[32] Karlsruhe Institute of Technology-Campus North-Institut für Kernphysik, Karlsruhe, Germany
[33] Bergische Universität Wuppertal, Wuppertal, Germany
[34] SUBATECH, École des Mines de Nantes, CNRS-IN2P3, Université de Nantes, France
[35] Max-Planck-Institut für Radioastronomie, Bonn, Germany
[36] Universidad de Alcalá, Alcalá de Henares, Madrid, Spain
[37] Institute of Physics of the Academy of Sciences of the Czech Republic, Prague, Czech Republic
[38] Università di Roma II "Tor Vergata" and Sezione INFN, Rome, Italy
[39] Instituto de Física, Universidade Federal do Rio de Janeiro, Rio de Janeiro, RJ, Brazil
[40] Institute of Nuclear Physics PAN, Krakow, Poland
[41] Colorado State University, Fort Collins, CO, USA
[42] "Horia Hulubei" National Institute for Physics and Nuclear Engineering, Bucharest-Magurele, Romania
[43] Colorado State University, Pueblo, CO, USA
[44] School of Physics and Astronomy, University of Leeds, UK
[45] Universität Siegen, Siegen, Germany
[46] Universidad de Granada & C. A. F. P.E., Granada, Spain
[47] Case Western Reserve University, Cleveland, OH, USA
[48] Pennsylvania State University, University Park, PA, USA
[49] Università di Milano and Sezione INFN, Milan, Italy
[50] Università di Catania and Sezione INFN, Catania, Italy
[51] Istituto di Astrofisica Spaziale e Fisica Cosmica di Palermo (INAF), Palermo, Italy
[52] Dipartimento di Matematica e Fisica "E. De Giorgi" dell'Università del Salento and Sezione INFN, Lecce, Italy

[53] Università di Torino and Sezione INFN, Torino, Italy
[54] Michigan Technological University, Houghton, MI, USA
[55] Observatorio Pierre Auger, Malargüe, Argentina
[56] Nikhef, Science Park, Amsterdam, The Netherlands
[57] Enrico Fermi Institute, University of Chicago, Chicago, IL, USA
[58] Instituto de Astronomía y Física del Espacio (CONICET-UBA), Buenos Aires, Argentina
[59] Departamento de Física, FCEyN, Universidad de Buenos Aires y CONICET, Argentina
[60] Universidade Federal Fluminense, EEIMVR, Volta Redonda, RJ, Brazil
[61] Faculty Mendoza (CONICET/CNEA), National Technological University, Mendoza, Argentina
[62] Instituto de Física, Universidade de São Paulo, São Carlos, SP, Brazil
[63] Kernfysisch Versneller Instituut, University of Groningen, Groningen, The Netherlands
[64] Institut de Physique Nucléaire d'Orsay (IPNO), Université Paris 11, CNRS-IN2P3, Orsay, France
[65] Università dell'Aquila and INFN, L'Aquila, Italy
[66] Institute for Nuclear Science and Technology (INST), Hanoi, Vietnam
[67] III. Physikalisches Institut A, RWTH Aachen University, Aachen, Germany
[68] ASTRON, Dwingeloo, The Netherlands
[69] J. Stefan Institute, Ljubljana, Slovenia
[70] Laboratory for Astroparticle Physics, University of Nova Gorica, Slovenia
[71] Dipartimento di Fisica dell'Università and INFN, Genova, Italy
[72] University of Łódź, Łódź, Poland
[73] University of New Mexico, Albuquerque, NM, USA
[74] INFN, Laboratori Nazionali del Gran Sasso, Assergi (L'Aquila), Italy
[75] Universidade Estadual de Feira de Santana, Brazil
[76] RCPTM, Palacky University, Olomouc, Czech Republic
[77] Faculty of Mathematics and Physics, Institute of Particle and Nuclear Physics, Charles University, Prague, Czech Republic
[78] Louisiana State University, Baton Rouge, LA, USA
[79] Universität Hamburg, Hamburg, Germany
[80] Universidade Federal do ABC, Santo André, SP, Brazil
[81] Benemérita Universidad Autónoma de Puebla, Puebla, Mexico
[82] Universidad Michoacana de San Nicolas de Hidalgo, Morelia, Michoacan, Mexico
[83] Centro de Investigación y de Estudios Avanzados del IPN (CINVESTAV), México, Mexico
[84] Rudolf Peierls Centre for Theoretical Physics, University of Oxford, Oxford, UK
[85] University of Hawaii, Honolulu, HI, USA
[86] Instituto de Física de Rosario (IFIR)-CONICET/U. N.R. and Facultad de Ciencias Bioquímicas y Farmacéuticas U. N.R., Rosario, Argentina
[87] Centro de Investigaciones en Láseres y Aplicaciones, CITEDEF and CONICET, Argentina
[88] Instituto de Física Corpuscular, CSIC-Universitat de València, Valencia, Spain
[89] Northeastern University, Boston, MA, USA
[90] Universidade Federal da Bahia, Salvador, BA, Brazil
[91] University of Nebraska, Lincoln, NE, USA
[92] Colorado School of Mines, Golden, CO, USA
[93] Physics Department, University of Bucharest, Bucharest, Romania
[94] Argonne National Laboratory, Argonne, IL, USA
[95] Los Alamos National Laboratory, Los Alamos, NM, USA

ABSTRACT

A thorough search for large-scale anisotropies in the distribution of arrival directions of cosmic rays detected above 10^{18} eV at the Pierre Auger Observatory is presented. This search is performed as a function of both declination and right ascension in several energy ranges above 10^{18} eV, and reported in terms of dipolar and quadrupolar coefficients. Within the systematic uncertainties, no significant deviation from isotropy is revealed. Assuming that any cosmic-ray anisotropy is dominated by dipole and quadrupole moments in this energy range, upper limits on their amplitudes are derived. These upper limits allow us to test the origin of cosmic rays above 10^{18} eV from stationary Galactic sources densely distributed in the Galactic disk and predominantly emitting light particles in all directions.

Key words: astroparticle physics – cosmic rays

Online-only material: color figures

1. INTRODUCTION

Establishing the energy at which the intensity of extragalactic cosmic rays starts to dominate the intensity of Galactic ones would constitute an important step forward to provide further understanding on the origin of ultrahigh energy cosmic rays

(UHECRs). A time-honored theory is that the *ankle*, a hardening of the energy spectrum located at $\simeq 4$ EeV (Linsley 1963; Lawrence et al. 1991; Nagano et al. 1992; Bird et al. 1993; The Pierre Auger Collaboration 2010a; where 1 EeV $\equiv 10^{18}$ eV), is the feature in the energy spectrum marking the transition between Galactic and extragalactic UHECRs (Linsley 1963). As a natural signature of the escape of cosmic rays from the Galaxy, large-scale anisotropies in the distribution of arrival directions could be detected at energies below this spectral feature. Both the amplitude and the shape of such patterns are uncertain as they depend on the model adopted to describe the regular and turbulent components of the Galactic magnetic field, the charges of the cosmic rays, and the assumed distribution of sources in

---

[96] Deceased.
[97] Now at University of Maryland.
[98] Now at Université de Lausanne.
[99] Also at Konan University, Kobe, Japan.
[100] Now at NYU Abu Dhabi.
[101] Now at the Universidad Autonoma de Chiapas on leave of absence from Cinvestav.

space and time. For cosmic rays that are mostly heavy and originate from stationary sources located in the Galactic disk, some estimates are based on diffusion and drift motions (Ptuskin et al. 1993; Candia et al. 2003) as well as direct integration of trajectories (Zirakashvili et al. 1998; Giacinti et al. 2012), which show that dipolar anisotropies at the level of a few percent could be imprinted in the energy range just below the ankle energy. Even larger amplitudes could result in light primaries, unless sources are strongly intermittent and pure diffusion motions hold up to EeV energies (Calvez et al. 2010; Eichler & Pohl 2011).

If UHECRs above 1 EeV have a predominant extragalactic origin (Hillas 1967; Blumenthal 1970; Berezinsky et al. 2006, 2004), their angular distribution is expected to be isotropic to a high level. But, even for isotropic extragalactic cosmic rays, the translational motion of the Galaxy relative to a possibly stationary extragalactic cosmic-ray rest frame can produce a dipole in a similar way to the Compton–Getting effect (Compton & Getting 1935), which has been measured with cosmic rays of much lower energy at the solar timescale (Cutler & Groom 1986; Amenomori et al. 2006; Abdo et al. 2009; Aglietta et al. 2009; Abbasi et al. 2010a) as a result of Earth's motion relative to the frame in which the cosmic rays have no bulk motion. Moreover, the rotation of the Galaxy can also produce anisotropy by virtue of moving magnetic fields, as cosmic rays traveling through far away regions of the Galaxy experience an electric force due to the relative motion of the system in which the field is purely magnetic (Harari et al. 2010). The large-scale structure of the Galactic magnetic field is expected to transform even a simple Compton–Getting dipole into a more complex anisotropy at Earth, described by higher order multipoles (Harari et al. 2010). A quantitative estimate of the imprinted pattern would require knowledge of the global structure of the Galactic magnetic field and the charges of the particles, as well as the frame in which extragalactic cosmic rays have no bulk motion. If, for instance, the frame in which the UHECR distribution is isotropic coincides with the cosmic microwave background rest frame, the amplitude of the simple Compton–Getting dipole would be about 0.6% (Kachelriess & Serpico 2006). The same order of magnitude is expected if UHECRs have no bulk motion with respect to the Local Group of galaxies.

The large-scale distribution of arrival directions of UHECRs as a function of the energy is thus one important observable to provide key elements for understanding their origin in the EeV energy range. Using the large amount of data collected by the Surface Detector (SD) array of the Pierre Auger Observatory, results of first harmonic analyses of the right ascension distribution performed in different energy ranges above 0.25 EeV were recently reported (The Pierre Auger Collaboration 2011a). Upper limits on the dipole component in the equatorial plane were derived, being below 2% at 99% CL for EeV energies and providing the most stringent bounds ever obtained. These analyses benefit from the almost uniform directional exposure in right ascension of the SD array of the Pierre Auger Observatory, which is due to Earth's rotation, and they constitute a powerful tool for picking up any dipolar modulation in this coordinate. However, since this technique is not sensitive to a dipolar component along Earth's rotation axis, in the present report we aim to estimate not only the dipole component in the right ascension distribution but also the component along Earth's rotation axis. More generally, we present a comprehensive search in all directions for any dipole or quadrupole patterns significantly standing out above the background noise.

Searching for anisotropies with relative amplitudes down to the percent level requires control of the exposure of the experiment at even greater accuracy. Spurious modulations in the right ascension distribution are induced by the variations of the effective size of the SD array with time and by the variations of the counting rate of events due to the changes of atmospheric conditions. In The Pierre Auger Collaboration (2011a), we showed in a quantitative way that such effects can be properly accounted for by making use of the instantaneous status of the SD array provided each second by the monitoring system, and by converting the observed signals in actual atmospheric conditions into ones that would have been measured at given reference atmospheric conditions. Searching for anisotropies explicitly in declination requires the control of additional systematic errors affecting both the directional exposure of the Observatory and the counting rate of events in local angles. Each of these additional effects is carefully presented in Sections 3 and 4.

After correcting for the experimental effects, searches for large-scale patterns above 1 EeV are presented in Section 5. Additional cross-checks against eventual systematic errors affecting the results obtained in Section 5 are presented in Section 6. Resulting upper limits on dipole and quadrupole amplitudes are presented and discussed in Section 7, while a final summary is given in Section 8. Some further technical aspects are detailed in Appendices A–D.

2. THE PIERRE AUGER OBSERVATORY AND THE DATA SET

The Pierre Auger Observatory (The Pierre Auger Collaboration 2004), located in Malargüe, Argentina, at mean latitude 35.2° S, mean longitude 69.5° W, and mean altitude 1400 m above sea level, has been designed to collect UHECRs with unprecedented statistics. It exploits two available techniques to detect extensive air showers initiated by cosmic-ray interactions in the atmosphere: a *surface detector array* and a *fluorescence detector*. The SD array consists of 1660 water-Cherenkov detectors laid out over about 3000 km² on a triangular grid with 1.5 km spacing. These water-Cherenkov detectors are sensitive to the light emitted in their volume by the secondary particles of the showers and provide a lateral sampling of the showers reaching the ground level. At the perimeter of this array, the atmosphere is observed on dark nights by 27 optical telescopes grouped in five buildings. These telescopes record the number of secondary charged particles in the air shower as a function of depth in the atmosphere by measuring the amount of nitrogen fluorescence caused by those particles along the track of the shower.

The analyses presented in this report make use of events recorded by the SD array from 2004 January 1 to 2011 December 31, with zenith angles less than 55°. To ensure good angle and energy reconstructions, each event must satisfy a fiducial cut requiring that the *elemental cell* of the event (that is, all six neighbors of the water-Cherenkov detector with the highest signal) was active when the event was recorded (The Pierre Auger Collaboration 2010b). Based on this fiducial cut, and accounting for unavoidable periods of array instability slightly reducing the duty cycle, the total geometric exposure corresponding to the data set considered in this report is 23,520 km² yr sr. This geometric exposure applies to energies at which the SD array operates with full detection efficiency, that is, to energies above 3 EeV (The Pierre Auger Collaboration 2010b).

The event direction is determined following the procedure described in Bonifazi et al. (2008). At the lowest energies observed, the angular resolution of the SD is about $2°.2$ and reaches $\sim 1°$ at the highest energies (Bonifazi et al. 2009). This is sufficient to perform searches for large-scale anisotropies.

The energy estimation of each event is primarily based on the measurement of the signal at a reference distance of 1000 m, $S(1000)$, referred to as the shower size. For a given energy, the shower size is a function of the zenith angle, due to the rapid increase of the slant depth, which induces an attenuation of the electromagnetic component of the showers. To account for this attenuation, the relationship between the observed $S(1000)$ and the one that would have been measured had the shower arrived at a zenith angle $38°$ is derived in an empirical way, using the constant intensity cut method (Hersil 1961). To convert $S_{38°}$ into energy, a calibration curve is used, based on events measured simultaneously by the SD array and the fluorescence telescopes (The Pierre Auger Collaboration 2008), since these telescopes indeed provide a calorimetric measurement of the energy. The statistical uncertainty of this energy estimation amounts to about 15%, while the absolute energy scale has a systematic uncertainty of 22% (The Pierre Auger Collaboration 2008).

3. CONTROL OF THE EVENT COUNTING RATE

The control of the event counting rate is critical in searches for large-scale anisotropies. Due to the steepness of the energy spectrum, any mild bias in the estimate of the shower energy with time or incident angles can lead to significant distortions of the event counting rate. The procedure followed to obtain an unbiased estimate of the shower energy is described in this section. This procedure consists of correcting measurements of shower sizes, $S(1000)$, for the influence of weather effects and the geomagnetic field *before* the conversion to $S_{38°}$ using the constant intensity method. Then, the conversion to energy is applied.

3.1. Influence of Atmospheric Conditions on Shower Size

The energy estimator of the showers recorded by the SD array is provided by the signal at 1000 m from the shower core, $S(1000)$. For any fixed energy, since the development of extensive air showers depends on the atmospheric pressure P and air density ρ, the corresponding $S(1000)$ is sensitive to variations in pressure and air density. Systematic variations with time of $S(1000)$ induce variations of the event rate that may distort the real dependence of the cosmic-ray intensity with right ascension. To cope with this experimental effect, the observed shower size $S(1000)$, measured at the actual density ρ and pressure P, is related to the one $S_{atm}(1000)$ that would have been measured at reference values ρ_0 and P_0 (The Pierre Auger Collaboration 2009):

$$S_{atm}(1000) = [1 - \alpha_P(\theta)(P - P_0) - \alpha_\rho(\theta)(\rho_d - \rho_0)$$
$$- \beta_\rho(\theta)(\rho - \rho_d)]S(1000). \quad (1)$$

The reference values are chosen as the average values at Malargüe (i.e., $\rho_0 = 1.06$ kg m^{-3} and $P_0 = 862$ hPa). ρ_d denotes here the average daily density at the time the event was recorded. The measured coefficients α_ρ, β_ρ and α_P—given in Table 1—give the influence on the shower sizes of the air density (and thus temperature) at long and short timescales on the Molière radius (and hence the lateral profiles of the

Table 1
Coefficients α_ρ, β_ρ, and α_P Used to Correct Shower Sizes for Atmospheric Effects on Shower Development, in Bins of sec θ

sec θ	α_ρ(kg^{-1} m^3)	β_ρ(kg^{-1} m^3)	α_P(h Pa^{-1})
[1.0–1.2]	$-9.7\ 10^{-1}$	$-2.6\ 10^{-1}$	$-4.4\ 10^{-4}$
[1.2–1.4]	$-7.2\ 10^{-1}$	$-2.2\ 10^{-1}$	$-1.6\ 10^{-3}$
[1.4–1.6]	$-5.4\ 10^{-1}$	$-2.0\ 10^{-1}$	$-2.3\ 10^{-3}$
[1.6–1.8]	$-4.0\ 10^{-1}$	$-4.3\ 10^{-2}$	$-1.9\ 10^{-3}$
[1.8–2.0]	$-1.5\ 10^{-1}$	$-2.3\ 10^{-2}$	$-2.8\ 10^{-3}$

Note. From The Pierre Auger Collaboration (2009).

showers) and of the pressure on the longitudinal development of air showers, respectively.

Applying these corrections to the energy assignments of showers allows us to cancel spurious variations of the event rate in right ascension, where typical amplitudes amount to a few per thousand when considering data sets collected over full years.

3.2. Influence of the Geomagnetic Field on Shower Size

The trajectories of charged particles in extensive air showers are curved in Earth's magnetic field, resulting in a broadening of the spatial distribution of particles in the direction of the Lorentz force. As the strength of the geomagnetic field component perpendicular to any arrival direction depends on both the zenith and azimuthal angles, the small changes of the density of particles at ground induced by the field break the circular symmetry of the lateral spread of the particles and thus induce a dependence of the shower size $S(1000)$ at a fixed energy in terms of the azimuthal angle. Due to the steepness of the energy spectrum, such an azimuthal dependence translates into azimuthal modulations of the estimated cosmic-ray event rate at a given $S(1000)$. To eliminate these effects, the observed shower size $S(1000)$ is related to the one that would have been observed in the absence of geomagnetic field $S_{geom}(1000)$ (The Pierre Auger Collaboration 2011b):

$$S_{geom}(1000) = \left[1 - g_1 \cos^{-g_2}(\theta) \sin^2(\widehat{\mathbf{u}, \mathbf{b}})\right] S(1000), \quad (2)$$

where $g_1 = (4.2 \pm 1)10^{-3}$, $g_2 = 2.8 \pm 0.3$, and $\mathbf{u}$ and $\mathbf{b} = \mathbf{B}/\|\mathbf{B}\|$ denote the unit vectors in the shower direction and the geomagnetic field direction, respectively. At a zenith angle $\theta = 55°$, the amplitude of the asymmetry in azimuth already amounts to $\simeq 2\%$, which is why we restrict the present analysis to zenith angles smaller than this value. Carrying out these corrections is thus critical for performing large-scale anisotropy measurements in declination.

3.3. From Shower Size to Energy

Once the influence on $S(1000)$ of weather and geomagnetic effects are accounted for, the dependence of $S(1000)$ on zenith angle, due to the attenuation of the shower and geometrical effects, is extracted from the data using the constant intensity cut method (The Pierre Auger Collaboration 2008). The attenuation curve $CIC(\theta)$ is fitted with a second-order polynomial in $x = \cos^2(\theta) - \cos^2(38°)$: $CIC(\theta) = 1 + ax + bx^2$. The angle $38°$ is chosen as a reference to convert $S(1000)$ to $S_{38°} = S(1000)/CIC(\theta)$. $S_{38°}$ may be regarded as the signal that would have been expected had the shower arrived at $38°$. The values of the parameters $a = 0.94 \pm 0.03$ and $b = -0.95 \pm 0.05$

are deduced for $S_{38°} = 22$ VEM,[102] which corresponds to an energy of about 4 EeV—just above the threshold energy for full efficiency. The differences between these parameters and previous reports will be discussed in Section 6.

Finally, the sub-sample of events recorded by both the fluorescence telescopes and the SD array is used to establish the relationship between the energy reconstructed with the fluorescence telescopes E_{FD} and $S_{38°}$: $E_{FD} = A S_{38°}^{B}$. The resulting parameters from the data fit are $A = (1.68 \pm 0.05) \times 10^{-1}$ EeV and $B = 1.030 \pm 0.009$, in good agreement with the recent report given in Pesce et al. (2011). The energy scale inferred from this data sample is applied to all showers detected by the SD array.

4. DIRECTIONAL EXPOSURE OF THE SURFACE DETECTOR ARRAY ABOVE 1 EeV

The *directional exposure* ω of the Observatory provides the effective time-integrated collecting area for a flux from each direction of the sky,[103] in units of km^2 yr. For energies below 3 EeV, it is controlled by the detection efficiency ϵ for triggering. This efficiency depends on the energy E, the zenith angle θ, and the azimuth angle φ. Consequently, the directional exposure of the Observatory is maximal above 3 EeV, and it is smaller at lower energies where the detection efficiency is less than unity.

In this section, we show in a comprehensive way how the directional exposure of the SD array is obtained as a function of the energy. We first explain how the slightly non-uniform exposure of the sky in sidereal time can be accounted for in the search for anisotropies (Section 4.1). In Section 4.2, we empirically calculate the detection efficiency as a function of the zenith angle and deduce the exposure below the full efficiency energy (3 EeV). In Section 4.3, we discuss the azimuthal dependence of the efficiency due to the geomagnetic effects, introduce the corrections due to the tilt of the array in Section 4.4 and the corrections due to the spatial extension of the array in Section 4.5 and show that the influence of weather effects is negligible on the detection efficiency between 1 and 3 EeV in Section 4.6. Finally we give in Section 4.7 some examples of our fully corrected exposure at several energies.

4.1. From Local to Celestial Directional Exposure

The choice of the fiducial cut to select high-quality events allows the precise determination of the geometric directional aperture per cell as $a_{cell}(\theta) = 1.95 \cos \theta$ km^2 (The Pierre Auger Collaboration 2010b). It also allows us to exploit the regularity of the array for obtaining its geometric directional aperture as a simple multiple of $a_{cell}(\theta)$ (The Pierre Auger Collaboration 2010b). The number of elemental cells $n_{cell}(t)$ is accurately monitored every second at the Observatory. To search for celestial large-scale anisotropies, it is mandatory to account for the modulation imprinted by the variations of $n_{cell}(t)$ in the expected number of events at the *sidereal periodicity* T_{sid}. Within each sidereal day, and in the same way as in The Pierre Auger Collaboration (2011a), we denote by α^0 the local sidereal time and express it in hours or in radians, as appropriate. For practical reasons, α^0 is chosen so that it is always equal to the right ascension of the zenith at the center of the array. As a

function of α^0, the total number of elemental cells $N_{cell}(\alpha^0)$ and its associated relative variations $\Delta N_{cell}(\alpha^0)$ are then obtained from

$$N_{cell}(\alpha^0) = \sum_j n_{cell}(\alpha^0 + jT_{sid}), \quad \Delta N_{cell}(\alpha^0) = \frac{N_{cell}(\alpha^0)}{\langle N_{cell}\rangle_{\alpha^0}},$$
(3)

with $\langle N_{cell}\rangle_{\alpha^0} = 1/T_{sid} \int_0^{T_{sid}} d\alpha^0 N_{cell}(\alpha^0)$. In the same way as in The Pierre Auger Collaboration (2011a), the small modulation of the expected number of events in right ascension induced by those variations will be accounted for by weighting each event k with a factor inversely proportional to $\Delta N_{cell}(\alpha_k^0)$ when estimating the anisotropy parameters in Section 5. Placing such time dependences in the event weights allows us to remove the modulations in time imprinted by the growth of the array and the dead times for each detector.

At any time, the *effective* directional aperture of the SD array is controlled by the geometric one *and* by the detection efficiency function $\epsilon(\theta, \varphi, E)$. For each elemental cell, the directional exposure in celestial coordinates is then simply obtained through the integration over local sidereal time of $x^{(i)}(\alpha^0) \times a_{cell}(\theta) \times \epsilon(\theta, \varphi, E)$, where $x^{(i)}(\alpha^0)$ is the operational time of the cell (i). Actually, since the small modulations in time imprinted in the event counting rate by experimental effects will be accounted for by means of the weighting procedure just described when searching for anisotropies, the small variations in local sidereal time for each $x^{(i)}(\alpha^0)$ can be neglected in calculating ω. The zenith and azimuth angles are related to the declination and the right ascension through

$$\cos\theta = \sin\delta \sin\ell_{site} + \cos\delta \cos\ell_{site} \cos(\alpha - \alpha^0),$$
$$\tan\varphi = \frac{\cos\delta \sin\ell_{site} \cos(\alpha - \alpha^0) - \sin\delta \cos\ell_{site}}{\cos\delta \sin(\alpha - \alpha^0)}, \quad (4)$$

with ℓ_{site} the mean latitude of the Observatory. Since both θ and φ depend only on the difference $\alpha - \alpha^0$, the integration over α^0 can then be substituted for an integration over the hour angle $\alpha' = \alpha - \alpha^0$ so that the directional exposure actually does not depend on right ascension when the $x^{(i)}$ are assumed local sidereal time independent:

$$\omega(\delta, E) = \sum_{i=1}^{n_{cell}} x^{(i)} \int_0^{24h} d\alpha' \, a_{cell}(\theta(\alpha', \delta))$$
$$\times \epsilon(\theta(\alpha', \delta), \varphi(\alpha', \delta), E). \quad (5)$$

Above 3 EeV, this integration can be performed analytically (Sommers 2001). Below 3 EeV, the non-saturation of the detection efficiency makes the directional exposure lower. The next sections are dedicated to the determination of $\epsilon(\theta, \varphi, E)$.

4.2. Detection Efficiency

To determine the detection efficiency function, a natural method would be to generate showers by means of Monte Carlo simulations and to calculate the ratio of the number of triggered events to the total simulated. However, there are discrepancies in the predictions of the hadronic interaction model regarding the number of muons in shower simulations and what is found in our data (Engel et al. 2007). This prevents us from relying on this method for obtaining the detection efficiency to the required accuracy.

We adopt here instead an empirical approach, based on the quasi-invariance of the zenithal distribution to large-scale

---

[102] A vertical equivalent muon, or VEM, is the expected signal in a surface detector crossed by a muon traveling vertically and centrally to it.
[103] In other contexts, such as the determination of the energy spectrum for instance, the term "exposure" refers to the *total* exposure integrated over the celestial sphere, in units km^2 yr sr.
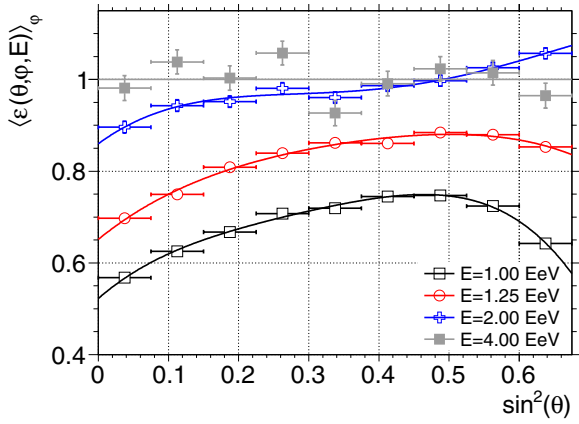
Figure 1. Detection efficiency averaged over the azimuth as a function of $\sin^2\theta$ at different energies, empirically measured from the data.

(A color version of this figure is available in the online journal.)

anisotropies for zenith angles less than $\simeq 60°$ and for any Observatory whose latitude is far from the poles of the Earth. For full efficiency, the distribution in zenith angles $dN/d\theta$ is proportional to $\sin\theta \cos\theta$ for solid angle and geometry reasons, so that the distribution in $dN/d\sin^2\theta$ is uniform. Consequently, below full efficiency, *any significant deviation from a uniform behavior in the $dN/d\sin^2\theta$ distribution provides an empirical measurement of the zenithal dependence of the detection efficiency*. The quasi-invariance of $dN/d\sin^2\theta$ to large-scale anisotropies is demonstrated in Appendix A.

Based on this quasi-invariance, the detection efficiency averaged over the azimuth can be estimated from

$$\langle \epsilon(\theta,\varphi,E)\rangle_\varphi = \frac{1}{\mathcal{N}}\frac{dN(\sin^2\theta,E)}{d\sin^2\theta}, \qquad (6)$$

where the notation $\langle\cdot\rangle_\varphi$ stands for the average over φ and the constant $\mathcal{N}$ is the number of events that would have been observed at energy E and for any $\sin^2\theta$ value in case of full efficiency for an energy spectrum $dN/dE = 40(E/\text{EeV})^{-3.27}$ km^{-2} yr^{-1} sr^{-1} EeV^{-1}—as measured between 1 and 4 EeV (The Pierre Auger Collaboration 2010a). Consequently, for each zenith angle, this empirical measurement of the efficiency provides an estimate *relative* to the overall spectrum of cosmic rays. In particular, since it is applied to *all* events detected at energy E without distinction based on the primary mass of cosmic rays, this technique does not provide the mass dependence of the detection efficiency. For that reason, the anisotropy searches reported in Section 5 pertain to the whole population of cosmic rays, whether this population consists of a single primary mass or a mixture of several elements.

Results are shown in Figure 1 for four different energies.[104] At 4 EeV, a uniform behavior around 1 is observed, though it is quite noisy due to the reduced statistics. This uniform behavior is consistent with full efficiency at this energy, as expected. Note that some values are greater than 1 for energies close to or higher than 3 EeV because of the empirical method of measuring the efficiency relative to the overall spectrum of cosmic rays. At 2 EeV, a loss of efficiency is observed for vertical showers due to the attenuation of the electromagnetic component of

the showers. Up to $\simeq 40°$, the detection efficiency steadily increases because the projected area of showers at ground gets larger with zenith angle. Above $\simeq 40°$, the rapid increase of the slant depth then makes the attenuation of the electromagnetic component stronger, but the muonic component of showers becomes dominant and ensures a high detection efficiency. At lower energies, the number of muons is, in contrast, too low to significantly impact the detection efficiency above $\simeq 40°–45°$, so that a clear decrease is observed at high zenith angles. In the following, we use parameterizations obtained by fitting each distribution with a fourth-order polynomial function in $\sin^2\theta$, which is sufficient to reproduce the main details as illustrated in Figure 1.

4.3. Geomagnetic Effects Below Full Efficiency

In addition to the effects on the energy determination presented in Section 3.2, geomagnetic effects also affect the detection efficiency for showers with energies below 3 EeV. This is because under any incident angles (θ,φ), a shower with an energy E triggers the SD array with a probability associated with its size which is a function of azimuth because of the geomagnetic effects[105]: $E \times (1 + \Delta(\theta,\varphi))^B$. Above 1 EeV, this effect is in fact the main source of azimuthal dependence of the detection efficiency, so that to first order in $\Delta(\theta,\varphi)$, $\epsilon(\theta,\varphi,E)$ can be estimated as

$$\epsilon(\theta,\varphi,E) = \frac{1}{\mathcal{N}}\frac{dN(\sin^2\theta, E(1+\Delta(\theta,\varphi))^B)}{d\sin^2\theta}$$
$$\simeq \langle\epsilon(\theta,\varphi,E)\rangle_\varphi + \frac{BE\Delta(\theta,\varphi)}{\mathcal{N}}\frac{\partial\langle\epsilon(\theta,\varphi,E)\rangle_\varphi}{\partial E}. \quad (7)$$

The correction to the detection efficiency induced by geomagnetic effects, and, in particular, the azimuthal dependence, is thus straightforward to implement from the knowledge of $\langle\epsilon(\theta,\varphi,E)\rangle_\varphi$. An example of such an azimuthal dependence is shown in the left panel of Figure 2, for $E = 1$ EeV and $\theta = 55°$. The modulation reflects the one due to the energy determination: the detection efficiency is lowered in the directions where the uncorrected energies are underestimated due to geomagnetic effects, and the efficiency is higher where energies are overestimated. The maximal contrast of such azimuthal modulations is displayed in the right panel as a function of the zenith angle, for three different energies. At 2 EeV, the amplitude slightly increases up to $\simeq 35°$, staying below $\simeq 0.1\%$, and then decreases and even cancels due to the saturation of the detection efficiency. In contrast, when decreasing in energy, the relative amplitude largely increases with the zenith angle due to the increase of the derivative term, reaching $\simeq 1.7\%$ for $\theta = 55°$ and $E = 1$ EeV.

4.4. Tilt of the Array

The altitudes above sea level of the water-Cherenkov detectors are displayed in Figure 3 with color coding. The coordinates are in a Cartesian system whose origin is defined at the "center" of the Observatory site. The Andes ridge building up in the western and northwestern direction can be seen. A slightly tilted SD array gives rise to a small azimuthal asymmetry, and consequently slightly modifies the directional exposure with respect

---

[104] To get the detection efficiency at a single energy E, events are actually selected in narrow energy bins around E. In addition, to account for the energy spectrum in $E^{-3.27}$ in this energy range, each event is weighted by a factor $E^{3.27}$.

[105] Here, the shorthand notation $\Delta(\theta,\varphi)$ stands for $g_1\cos^{-g_2}(\theta)[\sin^2(\widehat{\mathbf{u},\mathbf{b}}) - \langle\sin^2(\widehat{\mathbf{u},\mathbf{b}})\rangle_\varphi]$. The energy $E \times (1 + \Delta(\theta,\varphi))^B$ is actually the one that would have been obtained without correcting for geomagnetic effects.
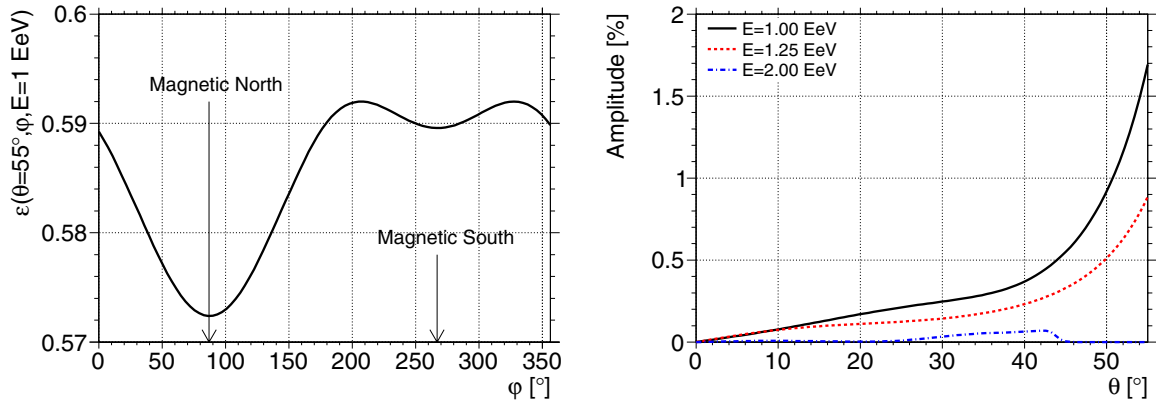
Figure 2. Left: dependence of the detection efficiency on azimuth for $\theta = 55°$ and $E = 1$ EeV due to geomagnetic effects. Right: maximal contrast of the azimuthal modulation of the detection efficiency induced by geomagnetic effects as a function of the zenith angle.

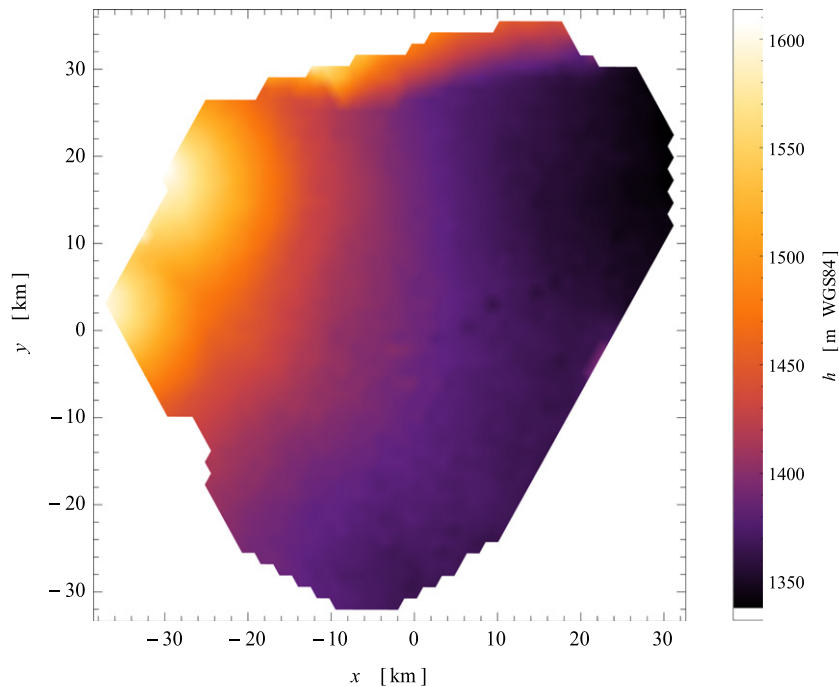(A color version of this figure is available in the online journal.)

Figure 3. Color-coded altitude (a.s.l.) of the water-Cherenkov detectors.

(A color version of this figure is available in the online journal.)

to Equation (5) through small changes of the geometric directional aperture. This modification is twofold: the tilt changes the geometric factor $(\cos \theta)$ of the projected surface under incidence angles (θ, φ) and also induces a compensating effect below full efficiency by slightly varying the detection efficiency with the azimuth angle φ.

Denoting $\mathbf{n}_{\perp}^{(\mathbf{i})}$ the normal vector to each elemental cell, the geometric directional aperture per cell is no longer simply given by $\cos \theta$ but now depends on both θ and φ:

$$a_{\text{cell}}^{(i)}(\theta, \varphi) = 1.95 \, \mathbf{n} \cdot \mathbf{n}_{\perp}^{(\mathbf{i})} \simeq 1.95$$
$$\times \left[1 + \zeta^{(i)} \tan \theta \cos \left(\varphi - \varphi_0^{(i)} \right) \right] \cos \theta, \quad (8)$$

where $\zeta^{(i)}$ and $\varphi_0^{(i)}$ are the zenith and azimuth angles of $\mathbf{n}_{\perp}^{(\mathbf{i})}$. It is actually this latter expression a_{cell} which has to be inserted into Equation (5) to calculate the directional exposure. Overall, the average tilt of the SD array is $\zeta^{\text{eff}} \simeq 0°\!.2$, and induces a

dipolar asymmetry in azimuth with a maximum in the downhill direction $\varphi_0^{\text{eff}} \simeq 0°$ and with an amplitude increasing with the zenith angle as $\simeq 0.3\% \tan \theta$.

Below 3 EeV, the tilt of the array induces an additional variation of the detection efficiency with azimuth. This is because the effective separation between detectors for a given zenith angle now depends on the azimuth. Since, for a given zenith angle, the SD array seen by showers coming from the uphill direction is denser than that for those coming from the downhill direction, the detection efficiency is higher in the uphill direction. Parameterizing the energy dependence of ϵ as $E^3/(E^3 + E_{0.5}^3)$, we show in Appendix B that the change in the detection efficiency can be estimated as

$$\Delta\epsilon_{\text{tilt}}(\theta, \varphi, E) = \frac{E^3 \left(E_{0.5}^3 - E_{0.5}^{\text{tilt}\,3}(\theta, \varphi) \right)}{\left(E^3 + E_{0.5}^3 \right) \left(E^3 + E_{0.5}^{\text{tilt}\,3}(\theta, \varphi) \right)}, \quad (9)$$
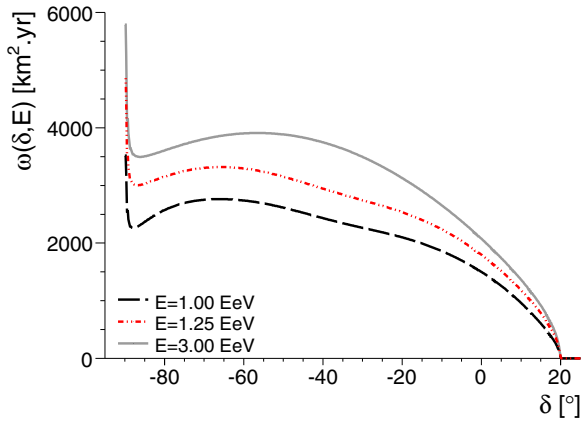
Figure 4. Directional exposure $\omega(\delta, E)$ as a function of the declination δ for three different energies.

(A color version of this figure is available in the online journal.)

where $E_{0.5}^{\mathrm{tilt}}(\theta, \varphi)$ is related to $E_{0.5}$ through

$$E_{0.5}^{\mathrm{tilt}}(\theta, \varphi) \simeq E_{0.5} \times \left[1 + \zeta^{\mathrm{eff}} \tan \theta \cos \left(\varphi - \varphi_0^{\mathrm{eff}}\right)\right]^{3/2}. \quad (10)$$

Around 1 EeV, this correction tends to compensate the pure geometrical effect described above, and even overcompensates it at lower energies.

4.5. Spatial Extension of the Array

This spatial extension of the SD array is such that the range of latitudes covered by all cells reaches $\simeq 0°.5$. This induces a slightly different directional exposure between the cells located at the northern part of the array and the ones located at the southern part. This spatial extension can be accounted for to calculate the overall directional exposure using the cell latitudes $\ell_{\mathrm{cell}}^{(i)}$ instead of the mean site one in the transformations from local to celestial angles in Equation (4).

4.6. Weather Effects below Full Efficiency

In the same way as geomagnetic effects, weather effects can also affect the detection efficiency for showers with energies below 3 EeV. However, *above* 1 EeV, we have shown in The Pierre Auger Collaboration (2011a) that as long as the analysis covers an integer number of years with almost equal exposure in every season, the amplitude of the spurious modulation in right ascension induced by this effect is small enough to be neglected when performing anisotropy analyses at the present level of sensitivity.

4.7. Final Estimation of the Directional Exposure—Examples at Some Energies

Accounting for all effects, the final expression to calculate the directional exposure is slightly modified with respect to Equation (5):

$$\omega(\delta, E) = \sum_{i=1}^{n_{\mathrm{cell}}} x^{(i)} \int_0^{24h} d\alpha' \, a_{\mathrm{cell}}^{(i)}(\theta, \varphi)$$
$$\times \left[\epsilon(\theta, \varphi, E) + \Delta\epsilon_{\mathrm{tilt}}(\theta, \varphi, E)\right], \quad (11)$$

where both θ and φ depend on α', δ, and $\ell_{\mathrm{cell}}^{(i)}$. The resulting dependence on declination is displayed in Figure 4 for three different energies. Down to 1 EeV, the detection efficiency at

high zenith angles is high enough that the equatorial south pole is visible at any time and hence constitutes the direction of maximum of exposure. For a wide range of declinations between $\simeq -89°$ and $\simeq -20°$, the directional exposure is $\simeq 2500$ km^2 yr at 1 EeV, and $\simeq 3500$ km^2 yr for any energy above full efficiency. Then, at higher declinations, it smoothly falls to zero, with no exposure above $\simeq 20°$ declination.

The average expected number of events within any solid angle and any energy range can be recovered by integrating the directional exposure over the solid angle considered and the cosmic-ray energy spectrum in the corresponding energy range. Note that the rapid variation of the exposure close to the South Pole on an angular scale of the order of the angular resolution has no influence on the event counting rate, due to the quasi-zero solid angle in that particular direction. Consequently, though the exposure around the South Pole could be affected by small changes of the detection efficiency around $\theta = 55°$, the results presented in next sections are on the other hand *not* affected by the exact value of the exposure for declinations a few degrees away from the South Pole.

5. SEARCHES FOR LARGE-SCALE PATTERNS

5.1. Estimates of Spherical Harmonic Coefficients

Any angular distribution over the sphere $\Phi(\mathbf{n})$ can be decomposed in terms of a multipolar expansion:

$$\Phi(\mathbf{n}) = \sum_{\ell \geqslant 0} \sum_{m=-\ell}^{\ell} a_{\ell m} Y_{\ell m}(\mathbf{n}), \quad (12)$$

where $\mathbf{n}$ denotes a unit vector taken in equatorial coordinates. The customary recipe to extract each multipolar coefficient makes use of the completeness relation of spherical harmonics:

$$a_{\ell m} = \int_{4\pi} d\Omega \Phi(\mathbf{n}) Y_{\ell m}(\mathbf{n}), \quad (13)$$

where the integration is over the entire sphere of directions $\mathbf{n}$. Any anisotropy fingerprint is encoded in the $a_{\ell m}$ spherical harmonic coefficients. Variations on an angular scale of Θ radians contribute amplitude in the $\ell \simeq 1/\Theta$ modes.

However, in the case of partial sky coverage, the solid angle in the sky where the exposure is zero makes it impossible to estimate the multipolar coefficients $a_{\ell m}$ in this way. This is because the unseen solid angle prevents one from making use of the completeness relation of the spherical harmonics (Sommers 2001). Since the observed arrival direction distribution is in this case the *combination* of the angular distribution $\Phi(\mathbf{n})$ and of the directional exposure function $\omega(\mathbf{n})$, the integration performed in Equation (13) does not allow any longer the extraction of the multipolar coefficients of $\Phi(\mathbf{n})$, but only the ones of $\omega(\mathbf{n})\Phi(\mathbf{n})$ (Billoir & Deligny 2008)[106]:

$$b_{\ell m} = \int_{\Delta\Omega} d\Omega \omega(\mathbf{n}) \Phi(\mathbf{n}) Y_{\ell m}(\mathbf{n})$$
$$= \sum_{\ell' \geqslant 0} \sum_{m'=-\ell'}^{\ell'} a_{\ell' m'} \int_{\Delta\Omega} d\Omega \omega(\mathbf{n}) Y_{\ell' m'}(\mathbf{n}) Y_{\ell m}(\mathbf{n}). \quad (14)$$

---

[106] To cope with the unseen solid angle, another approach makes use of orthogonal functions of increasing multipolarity, tailored to the exposure ω itself (Billoir & Deligny 2008). This method would yield similar accuracies.

Formally, the $a_{\ell m}$ coefficients appear related to the $b_{\ell m}$ ones through a convolution such that $b_{\ell m} = \sum_{\ell' \geqslant 0} \sum_{m'=-\ell'}^{\ell'} [K]_{\ell m}^{\ell' m'} a_{\ell' m'}$. The matrix K, which imprints the interferences between modes induced by the non-uniform and partial coverage of the sky, is entirely determined by the directional exposure. The relationship established in Equation (14) is valid for *any* exposure function $\omega(\mathbf{n})$.

Meanwhile, the observed arrival direction distribution, $\overline{dN}(\mathbf{n})/d\Omega$, provides a direct estimation of the $b_{\ell m}$ coefficients through (hereafter, we use an overline to indicate the *estimator* of any quantity)

$$\overline{b}_{\ell m} = \int_{\Delta\Omega} d\Omega \frac{\overline{dN}(\mathbf{n})}{d\Omega} Y_{\ell m}(\mathbf{n}), \qquad (15)$$

where the distribution $\overline{dN}(\mathbf{n})/d\Omega$ of any set of N arrival directions $\{\mathbf{n}_1, ..., \mathbf{n}_N\}$ can be modeled as a sum of Dirac functions on the sphere. Then, if the multipolar expansion of the angular distribution $\Phi(\mathbf{n})$ is *bounded* to ℓ_{max}, that is, if the $\Phi(\mathbf{n})$ has no higher moments than ℓ_{max}, the first $b_{\ell m}$ coefficients with $\ell \leqslant \ell_{max}$ are related to the non-vanishing $a_{\ell m}$ by the square matrix $K_{\ell_{max}}$ *truncated* to ℓ_{max}. Inverting this truncated matrix allows us to recover the underlying $a_{\ell m}$ from the measured $b_{\ell m}$ (with $\ell \leqslant \ell_{max}$):

$$\overline{a}_{\ell m} = \sum_{\ell'=0}^{\ell_{max}} \sum_{m'=-\ell'}^{\ell'} \left[K_{\ell_{max}}^{-1} \right]_{\ell m}^{\ell' m'} \overline{b}_{\ell' m'}. \qquad (16)$$

In the case of small anisotropies ($|a_{\ell m}|/a_{00} \ll 1$), the resolution on each recovered $\overline{a}_{\ell m}$ coefficient is proportional to ($[K_{\ell_{max}}^{-1}]_{\ell m}^{\ell m})^{0.5}$ (Billoir & Deligny 2008):

$$\sigma_{\ell m} = \left(\left[K_{\ell_{max}}^{-1} \right]_{\ell m}^{\ell m} \overline{a}_{00} \right)^{0.5}. \qquad (17)$$

The dependence on ℓ_{max} of the coefficients of $K_{\ell_{max}}^{-1}$ induces an intrinsic indeterminacy of each recovered coefficient $\overline{a}_{\ell m}$ as ℓ_{max} is increasing. This is nothing else but the mathematical translation of it being impossible to know the angular distribution of cosmic rays in the uncovered region of the sky.

Henceforth, we adapt this general formalism to the search for anisotropies in Auger data in different energy intervals. We assume that the energy dependence of the angular distribution of cosmic rays is smooth enough that the multipolar coefficients can be considered constant for any energy E within a narrow interval ΔE. The directional exposure is hereafter considered as independent of the right-ascension, as defined in Section 4. Within an energy interval ΔE, the expected arrival direction distribution thus reads

$$\frac{dN(\mathbf{n})}{d\Omega} \propto \tilde{\omega}(\delta) \sum_{\ell \geqslant 0} \sum_{m=-\ell}^{\ell} a_{\ell m} Y_{\ell m}(\mathbf{n}), \qquad (18)$$

where $\tilde{\omega}(\delta)$ is the effective directional exposure for the energy interval ΔE. For convenience, this latter function is normalized such that

$$\tilde{\omega}(\delta) = \frac{\displaystyle\int_{\Delta E} dE\, E^{-\gamma} \omega(\delta, E)}{\displaystyle\max_{\delta} \left[\int_{\Delta E} dE\, E^{-\gamma} \omega(\delta, E) \right]}, \qquad (19)$$

with γ the spectral index in the considered energy range. This dimensionless function provides, for any direction on the sky, the effective directional exposure in the energy range ΔE at that direction, *relative* to the largest directional exposure on the sky. This is actually the relevant quantity which enters into Equation (14) for the analyses presented below. Note that for a directional exposure independent of the right ascension, the coefficients $[K]_{\ell m}^{\ell' m'}$ are proportional to $\delta_m^{m'}$, i.e., different values of m are not mixed in the matrix. The observed arrival direction distribution, $\overline{dN}(\mathbf{n})/d\Omega$, is here modeled as a sum of Dirac functions on the sphere weighted by the factor $\Delta N_{cell}^{-1}(\alpha_k^0)$ for each event recorded at local sidereal time α_k^0, as described in Section 4.1 to correct for the slightly non-uniform directional exposure in right ascension. In this way, the integration in Equation (14) yields to

$$\overline{b}_{\ell m} = \sum_{k=1}^{N} \frac{Y_{\ell m}(\mathbf{n}_k)}{\Delta N_{cell}(\alpha_k^0)}. \qquad (20)$$

The multipolar coefficients $\overline{a}_{\ell m}$ are then recovered by means of Equation (16). Given the exposure functions described in Section 4, the resolution on each recovered coefficient, encoded in Equation (17), is degraded by a factor larger than 2 each time ℓ_{max} is increased by 1. This prevents the recovery of each coefficient with good accuracy as soon as $\ell_{max} \geqslant 3$, since, for $\ell_{max} = 3$ for instance, our current statistics would only allow us to probe dipole amplitudes at the 10% level. Consequently, in the following, we restrict ourselves to reporting results on individual coefficients obtained when assuming a dipolar distribution ($\ell_{max} = 1$) and a quadrupolar distribution ($\ell_{max} = 2$). Meanwhile, due to the interference between modes induced by the non-uniform and partial sky coverage, it is important to stress again that each multipolar coefficient recovered under the assumption of a particular bound ℓ_{max} might be biased if the underlying angular distribution of cosmic rays is not bounded to ℓ_{max}. Given the directional exposure functions considered in this study, this effect can be important only if the angular distribution has in fact significant moments of order $\ell_{max} + 1$.

5.2. Searches for Dipolar Patterns

As outlined in the Introduction, a measurable dipole is regarded as a likely possibility in many scenarios for the origin of cosmic rays at EeV energies. Assuming that the angular distribution of cosmic rays is modulated by a *pure* dipole, the intensity $\Phi(\mathbf{n})$ can be parameterized in any direction $\mathbf{n}$ as

$$\Phi(\mathbf{n}) = \frac{\Phi_0}{4\pi} (1 + r\mathbf{d} \cdot \mathbf{n}), \qquad (21)$$

where $\mathbf{d}$ denotes the dipole unit vector. The dipole pattern is here fully characterized by a declination δ_d, a right ascension α_d, and an *amplitude r* corresponding to the maximal anisotropy contrast:

$$r = \frac{\Phi_{max} - \Phi_{min}}{\Phi_{max} + \Phi_{min}}. \qquad (22)$$

The estimation of these three coefficients is straightforward from the estimated spherical harmonic coefficients $\overline{a}_{1m}$: $\overline{r} = [3(\overline{a}_{10}^2 + \overline{a}_{11}^2 + \overline{a}_{1-1}^2)]^{0.5}/\overline{a}_{00}$, $\overline{\delta} = \arcsin(\sqrt{3}\overline{a}_{10}/\overline{a}_{00}\overline{r})$, and $\overline{\alpha} = \arctan(\overline{a}_{1-1}/\overline{a}_{11})$. Uncertainties on $\overline{r}$, $\overline{\delta}$, and $\overline{\alpha}$ are obtained from the propagation of uncertainties on each recovered $\overline{a}_{1m}$ coefficient (cf. Equation (17)). Under an underlying isotropic
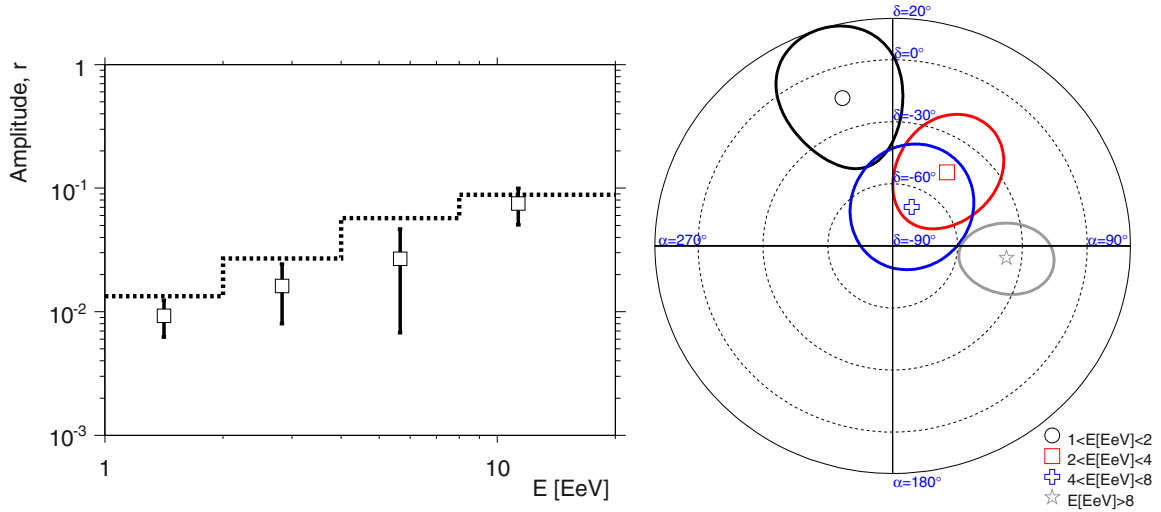
Figure 5. Left: reconstructed amplitude of the dipole as a function of energy. The dotted line stands for the 99% CL upper bounds on the amplitudes that would result from fluctuations of an isotropic distribution. Right: reconstructed declination and right ascension of the dipole with corresponding uncertainties, as a function of energy, in azimuthal projection.

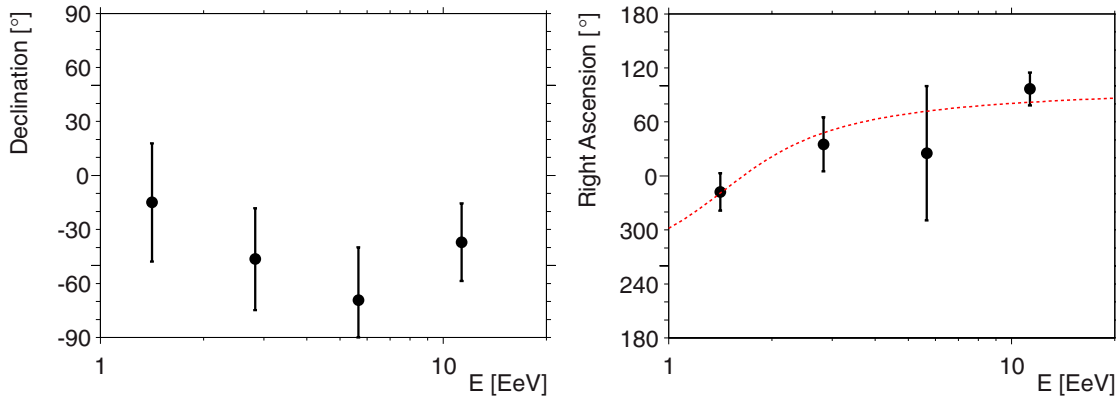(A color version of this figure is available in the online journal.)

Figure 6. Reconstructed declination (left) and right ascension (right) of the dipole as a function of energy. The smooth fit to the data of The Pierre Auger Collaboration (2011a) is shown as the dashed line in the right panel: a consistent smooth behavior is observed using the analysis presented here and applied to a data set containing two additional years of data.

(A color version of this figure is available in the online journal.)

distribution, and for an axisymmetric directional exposure around the axis defined by the North and South equatorial poles, the probability density function of $\overline{r}$ is given by (The Pierre Auger Collaboration 2011b):

$$p_R(\overline{r}) = \frac{\overline{r}}{\sigma\sqrt{\sigma_z^2 - \sigma^2}} \text{erfi}\left(\frac{\sqrt{\sigma_z^2 - \sigma^2}}{\sigma \sigma_z} \frac{\overline{r}}{\sqrt{2}}\right) \exp\left(-\frac{\overline{r}^2}{2\sigma^2}\right),$$
(23)

where $\text{erfi}(z) = \text{erf}(iz)/i$, $\sigma = \sqrt{3}\sigma_{11}/\overline{a}_{00}$, and $\sigma_z = \sqrt{3}\sigma_{10}/\overline{a}_{00}$. The probability $P_R(> \overline{r})$ that an amplitude equal to or larger than $\overline{r}$ arises from a statistical fluctuation of an isotropic distribution is then obtained by integrating p_R above $\overline{r}$:

$$P_R(> \overline{r}) = \text{erfc}\left(\frac{\overline{r}}{\sqrt{2}\sigma_z}\right) + \text{erfi}\left(\frac{\sqrt{\sigma_z^2 - \sigma^2}}{\sigma \sigma_z} \frac{\overline{r}}{\sqrt{2}}\right) \exp\left(-\frac{\overline{r}^2}{2\sigma^2}\right).$$
(24)

The reconstructed amplitudes $\overline{r}(E)$ and corresponding directions are shown in Figure 5 with the associated uncertainties, as a function of the energy. The directions are drawn in azimuthal projection, with the equatorial South Pole located at the center and the right ascension going from 0 to 360° clockwise. In the left panel, the 99% CL upper bounds on the amplitudes that

would result from fluctuations of an isotropic distribution are indicated by the dotted line (i.e., the amplitudes $\overline{r}_{99}(E)$ such that $P_R(> \overline{r}_{99}(E)) = 0.01$). One can see that within the statistical uncertainties, there is no strong evidence of any significant signal.

The reconstructed declinations $\overline{\delta}$ and right ascensions $\overline{\alpha}$ are shown separately in Figure 6. Both quantities are expected to be randomly distributed in case of independent samples whose parent distribution is isotropic. In our previous report on the first harmonic analysis in right ascension (The Pierre Auger Collaboration 2011a), we pointed out the intriguing smooth alignment of the phases in right ascension as a function of the energy, and noted that such a consistency of phases in adjacent energy intervals is expected to manifest with a smaller number of events than those required for the detection of amplitudes standing out significantly above the background noise in the case of a real underlying anisotropy. This motivated us to design a *prescription* aimed at establishing at 99% CL whether this consistency in phases is real, using the exact same analysis as the one reported in The Pierre Auger Collaboration (2011a). The prescribed test will end once the total exposure since 2011 June 25 reaches 21,000 km² yr sr. The smooth fit to the data of The Pierre Auger Collaboration (2011a) is shown as
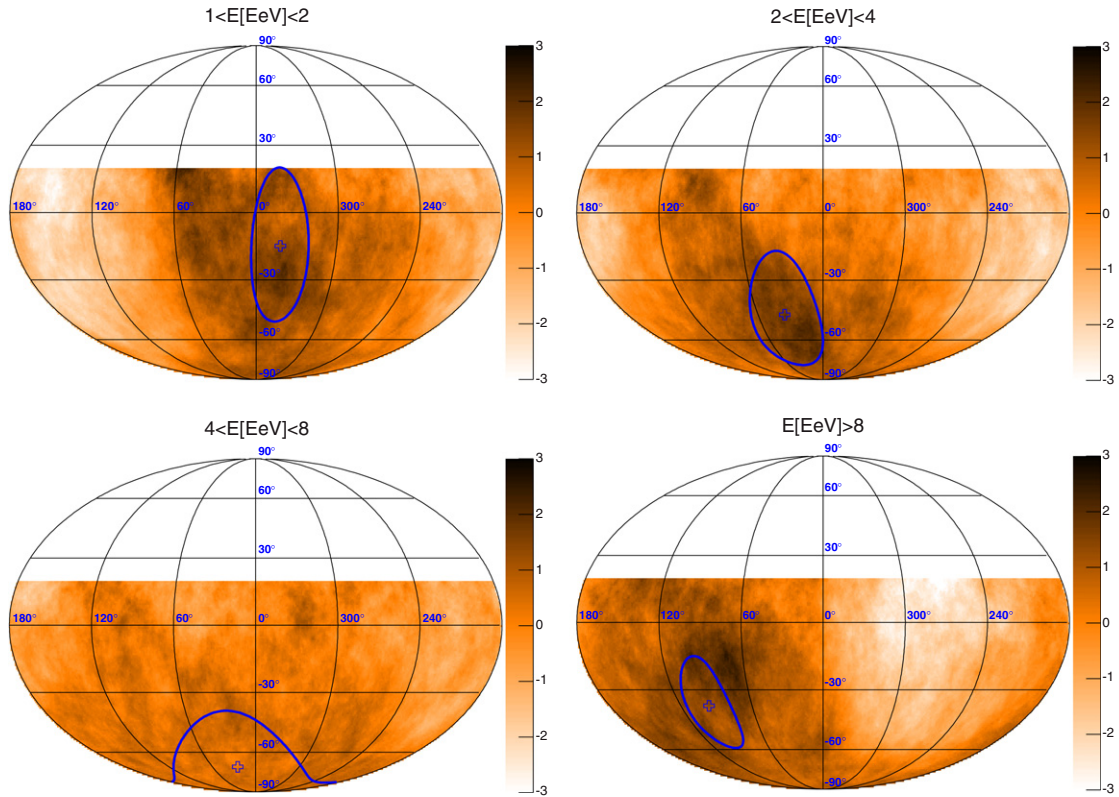
Figure 7. Significance sky maps in four independent energy bins. The maps are smoothed using an angular window with radius $\Theta = 1$ rad to exhibit any dipolar-like structures. The directions of the reconstructed dipoles are shown with the associated uncertainties. The Galactic plane and Galactic center are also depicted as the dotted line and the star.

(A color version of this figure is available in the online journal.)

a dashed line in the right panel of Figure 6, restricted to the energy range considered here. Though the phase between 4 and 8 EeV is poorly determined due to the corresponding direction in declination pointing close to the equatorial South Pole, it is noteworthy that a consistent smooth behavior is observed using the analysis presented here and applied to a data set containing two additional years of data. It is also interesting to see in the left panel that all reconstructed declinations are in the equatorial Southern Hemisphere.

For completeness, significance sky maps are displayed in Figure 7 in equatorial coordinates and using a Mollweide projection, for the four energy ranges. The Galactic plane and Galactic center are also depicted as the dotted line and the star. Significances are calculated using the Li and Ma estimator (Li & Ma 1983). This widely used estimator of significance, S, properly accounts for the fluctuations of the background and of an eventual signal in any angular region searched.[107] If no signal is present, the variable S is nearly normally distributed even for small count numbers, so that positive values of S can be interpreted as the number of standard deviations of any excess in the sky. Also, for negative values of S, $-S$ can be interpreted as the number of standard deviations of any deficit in the sky. The maps show the overdensities obtained in circular windows of radius $\Theta = 1$ radian, to better exhibit possible dipolar-like structures. The directions of the reconstructed dipoles are also shown, with their associated uncertainties (thick circles).

Finally, since some consistency is observed both in declination and right ascension as a function of energy, the use of larger energy intervals and/or energy thresholds may help to pick up a significant signal above the background level. The amplitudes of the dipole are shown in Figure 8 for two energy intervals ($1 < E/[\text{EeV}] < 4$ and $E > 4$ EeV) and as a function of energy thresholds. This does not provide any further evidence for significant anisotropies.

5.3. Searches for Quadrupolar Patterns

Any excesses along a plane would show up as a prominent quadrupole moment. Such excesses are plausible for instance at EeV energies in the case of an emission of light EeV cosmic rays from sources preferentially located in the Galactic disk, or at higher energies from sources preferentially located in the super-Galactic plane. Consequently, a measurable quadrupole may be regarded as an interesting outcome of an anisotropy search at ultrahigh energies.

Assuming now that the angular distribution of cosmic rays is modulated by a dipole *and* a quadrupole, the intensity $\Phi(\mathbf{n})$ can be parameterized in any direction $\mathbf{n}$ as

$$\Phi(\mathbf{n}) = \frac{\Phi_0}{4\pi}\left(1 + r\mathbf{d}\cdot\mathbf{n} + \frac{1}{2}\sum_{i,j}Q_{ij}n_i n_j\right), \qquad (25)$$

where $\mathbf{Q}$ is a traceless and symmetric second order tensor. Its five independent components are determined in a straightforward way from the $\ell = 2$ spherical harmonic coefficients a_{2m}. Denoting by $\lambda_+, \lambda_0, \lambda_-$ the three eigenvalues of $\mathbf{Q}/2$ (λ_+ being the highest one and λ_- the lowest one) and $\mathbf{q}_+, \mathbf{q}_0, \mathbf{q}_-$ the

---

[107] The parameter α_{LM} in the expression of the Li & Ma significance, expressing the expected ratio of the count numbers between the angular region searched (the *on-region*) and any background region if there is no signal in the on-region, is here taken as the ratio between the expected number of events in the on-region and the total number of events in the energy range considered.
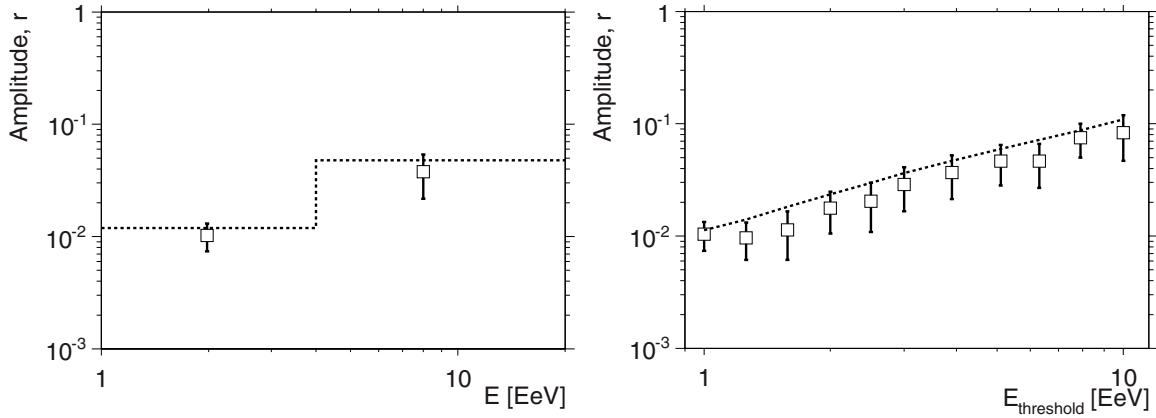
Figure 8. Left: amplitude of the dipole for two energy intervals: $1 < E/(\text{EeV}) < 4$ and $E > 4$ EeV. Right: amplitude of the dipole as a function of energy thresholds. The dotted lines stand for the 99% CL upper bounds on the amplitudes that could result from fluctuations of an isotropic distribution.

three corresponding unit eigenvectors, the intensity can be parameterized in a more intuitive way as

$$\Phi(\mathbf{n}) = \frac{\Phi_0}{4\pi}(1 + r\mathbf{d} \cdot \mathbf{n} + \lambda_+(\mathbf{q_+} \cdot \mathbf{n})^2 + \lambda_0(\mathbf{q_0} \cdot \mathbf{n})^2 + \lambda_-(\mathbf{q_-} \cdot \mathbf{n})^2). \tag{26}$$

It is then convenient to define the quadrupole amplitude β as

$$\beta \equiv \frac{\lambda_+ - \lambda_-}{2 + \lambda_+ + \lambda_-}. \tag{27}$$

In case of a pure quadrupolar distribution (i.e., in the absence of dipole), β is nothing else but the customary measure of maximal anisotropy contrast:

$$r = 0 \Rightarrow \beta = \frac{\lambda_+ - \lambda_-}{2 + \lambda_+ + \lambda_-} = \frac{\Phi_{\max} - \Phi_{\min}}{\Phi_{\max} + \Phi_{\min}}. \tag{28}$$

Hence, any quadrupolar pattern can be fully described by two amplitudes (β, λ_+) and three angles: (δ_+, α_+) which define the orientation of $\mathbf{q_+}$ and (α_-) which defines the direction of $\mathbf{q_-}$ in the orthogonal plane to $\mathbf{q_+}$. The third eigenvector $\mathbf{q_0}$ is orthogonal to $\mathbf{q_+}$ and $\mathbf{q_-}$, and its corresponding eigenvalue λ_0 is such that the traceless condition is satisfied: $\lambda_+ + \lambda_- + \lambda_0 = 0$. Though the probability density functions of the estimated quadrupole amplitudes $(\bar{\beta}, \bar{\lambda}_+)$ can be in principle calculated in the same way as in the case of the estimated dipole amplitude $(\bar{r})$, expressions are much more complicated to obtain even semi-analytically and we defer hereafter to Monte Carlo simulations to tabulate the distributions.

The amplitudes $\bar{r}(E)$, $\bar{\lambda}_+(E)$, and $\bar{\beta}(E)$ are shown in Figure 9 as functions of energy. Dipole amplitudes are compatible with expectations from isotropy. Compared to the results on the dipole obtained in previous section for $\ell_{\max} = 1$, the sensitivity is now degraded by a factor larger than 2 as expected from the dependence of the resolution $\sigma_{\ell m}$ on $\ell_{\max}$ (cf. Equation (17)). In the same way as for dipole amplitudes, the 99% CL upper bounds on the quadrupole amplitudes that could result from fluctuations of an isotropic distribution are indicated by the dashed lines. They correspond to the amplitudes $\bar{\lambda}_{+,99}(E)$ and $\bar{\beta}_{99}(E)$ such that the probabilities $P_{\Lambda_+}(> \bar{\lambda}_{+,99}(E))$ and $P_B(> \bar{\beta}_{99}(E))$ arising from statistical fluctuations of isotropy are equal to 0.01. Here, both distributions P_{Λ_+} and P_B are sampled from Monte Carlo simulations. Throughout the energy scan, there is no evidence for anisotropy. The largest deviation from isotropic expectations occurs between 2 and 4 EeV, where the amplitude $\bar{\lambda}_+$ lies just above $\bar{\lambda}_{+99}$.

Table 2
Influence of Shower Size Corrections for Geomagnetic Effects on the Component of the Dipole in the Equatorial Plane and on the One Along Earth's Rotation Axis

ΔE (EeV)	$\bar{r}_\perp^{\text{uncorr}}$ (%)	$\bar{r}_\perp$ (%)	$\bar{r}_\parallel^{\text{uncorr}}$ (%)	$\bar{r}_\parallel$ (%)
1–4	0.9 ± 0.3	0.9 ± 0.3	-2.2 ± 0.4	-1.0 ± 0.4
>4	1.8 ± 1.0	2.1 ± 1.0	-4.1 ± 1.7	-3.0 ± 1.7

6. ADDITIONAL CROSS-CHECKS AGAINST EXPERIMENTAL EFFECTS

6.1. More on the Influence of Shower Size Corrections for Geomagnetic Effects

Understanding the influence of the shower size corrections for geomagnetic effects is critical to get unbiased estimates of anisotropy parameters. Without accounting for these effects, an increase of the event rate would be observed close to the equatorial South Pole with respect to expectations for isotropy, while a decrease would be observed close to the edge of the directional exposure in the equatorial Northern Hemisphere. This would result in the observation of a fake dipole. A convenient way to exhibit this effect is to separate the dipole in two components : the component of the dipole in the equatorial plane $r_\perp$, and the component along Earth's rotation axis, $r_\parallel$. While $r_\perp$ is expected to be affected only by time-dependent effects, $r_\parallel$ is on the other hand the relevant quantity sensitive to time-independent effects such as the geomagnetic one.

Estimations of $r_\perp$ and $r_\parallel$ obtained by accounting or not for geomagnetic effects are given in Table 2, in two different energy ranges. These estimations are obtained from the recovered $\bar{a}_{1m}$ coefficients: $\bar{r}_\parallel = \sqrt{3}\bar{a}_{10}/\bar{a}_{00}$, and $\bar{r}_\perp = [3(\bar{a}_{11}^2 + \bar{a}_{1-1}^2)]^{0.5}/\bar{a}_{00}$. It can be seen that the main effect of the geomagnetic corrections is a shift in $\bar{r}_\parallel$ of about 1.2%. In the energy range $1 \leqslant E/\text{EeV} \leqslant 4$, this shift is significant, $\bar{r}_\parallel$ changing from -2.2% to -1.0% with an uncertainty amounting to 0.4%. Above 4 EeV, the net correction is of the same order, though the statistical uncertainties are larger. In contrast, $\bar{r}_\perp$ remains unchanged in both cases, as expected.

6.2. Eventual Energy Dependence of the Attenuation Curve

In this section, we study to which extent the procedure used to obtain the attenuation curve in Section 3.3 might influence the determination of the anisotropy parameters.
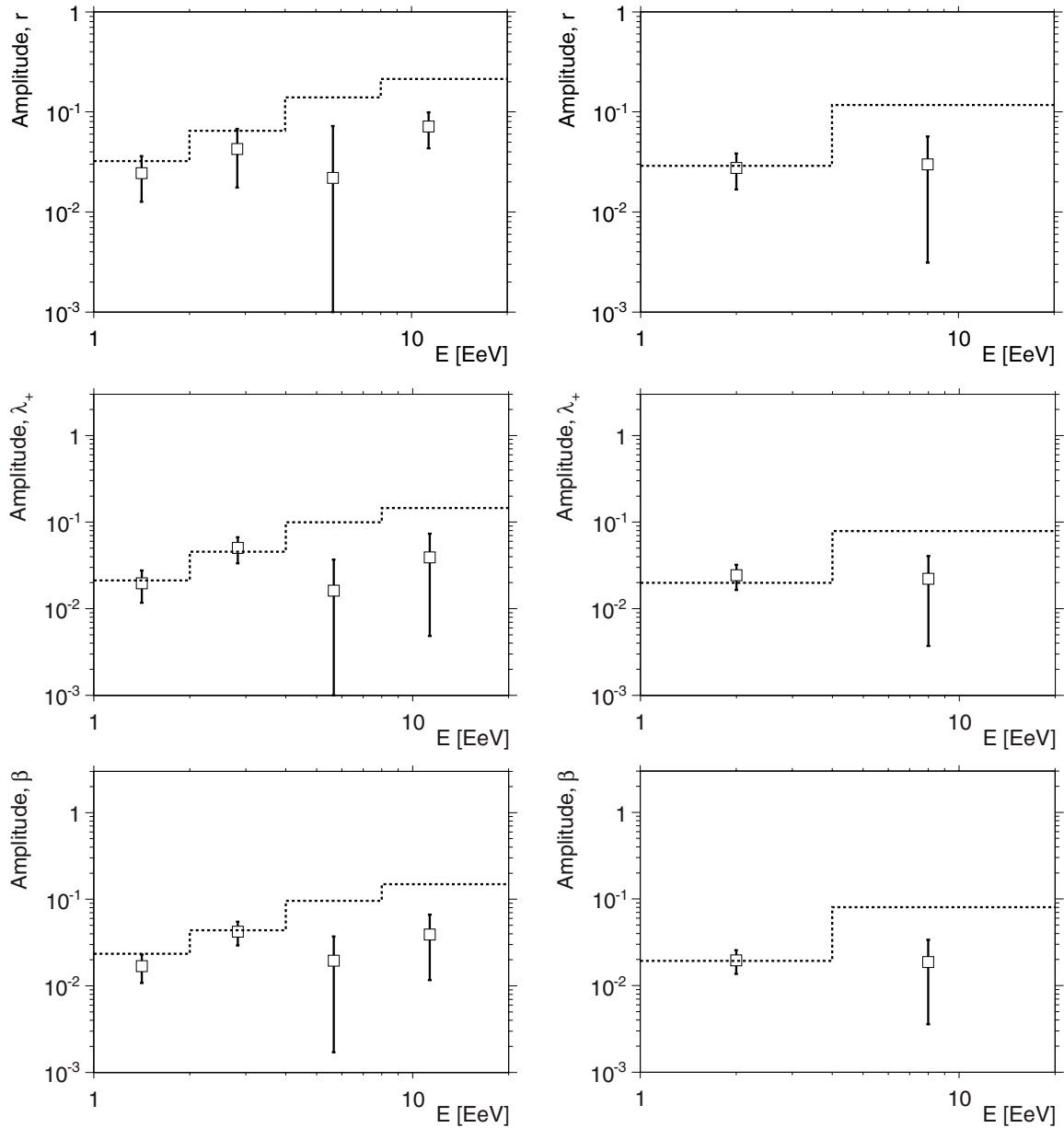
Figure 9. Amplitudes of the dipolar (top) and quadrupolar moments (middle and bottom) as a function of energy using a multipolar reconstruction up to $\ell_{max} = 2$ for two different binnings (left and right). In each panel, the dotted lines stand for the 99% CL upper bounds on the amplitudes that could result from fluctuations of an isotropic distribution.

To convert the shower size into energy, we explained and applied in Section 3.3 the constant intensity cut method for showers with $S_{38°} \geqslant 22 \text{VEM}$, that is, just above the threshold energy for full efficiency. The value of the parameter a obtained in these conditions is consistent within the statistical uncertainties with the one previously reported when applying the same constant intensity cut method for showers with $S_{38°} \geqslant 47 \text{VEM}$. Opposite to this, the value obtained for the coefficient b differs by more than three standard deviations. Such a difference might be expected from both the evolution of the maximum of the showers and from an eventual change in composition with energy, but it may also be due to energy- and angle-dependent resolution effects mimicking a real evolution with energy.

With a different attenuation curve, some events would be reconstructed in the adjacent energy intervals to an extent which depends on the change of the attenuation curve with zenith angle.

For that reason, the determination of anisotropy parameters might be altered by this effect.

Disentangling the real evolution of the attenuation curve from the energy from resolution effects is out of the scope of this paper and will be addressed elsewhere. Here, we restrict ourselves to probing the effect that a real energy dependence would have on the determination of anisotropy parameters. To do so, we choose to fit the values of the coefficient b obtained for $S_{38°} = 22 \text{VEM}$ and $S_{38°} = 47 \text{VEM}$ through a linear dependence with the logarithm of $S_{38°}$. Below and above these values, the behavior of $b(E)$ is obtained by *extrapolating* this energy dependence. In this way, the changes in the anisotropy parameters are probed in *extreme* conditions.

Repeating the whole chain of analysis with this new attenuation curve, it turns out that the reconstructed dipole parameters are only marginally affected by this change, as
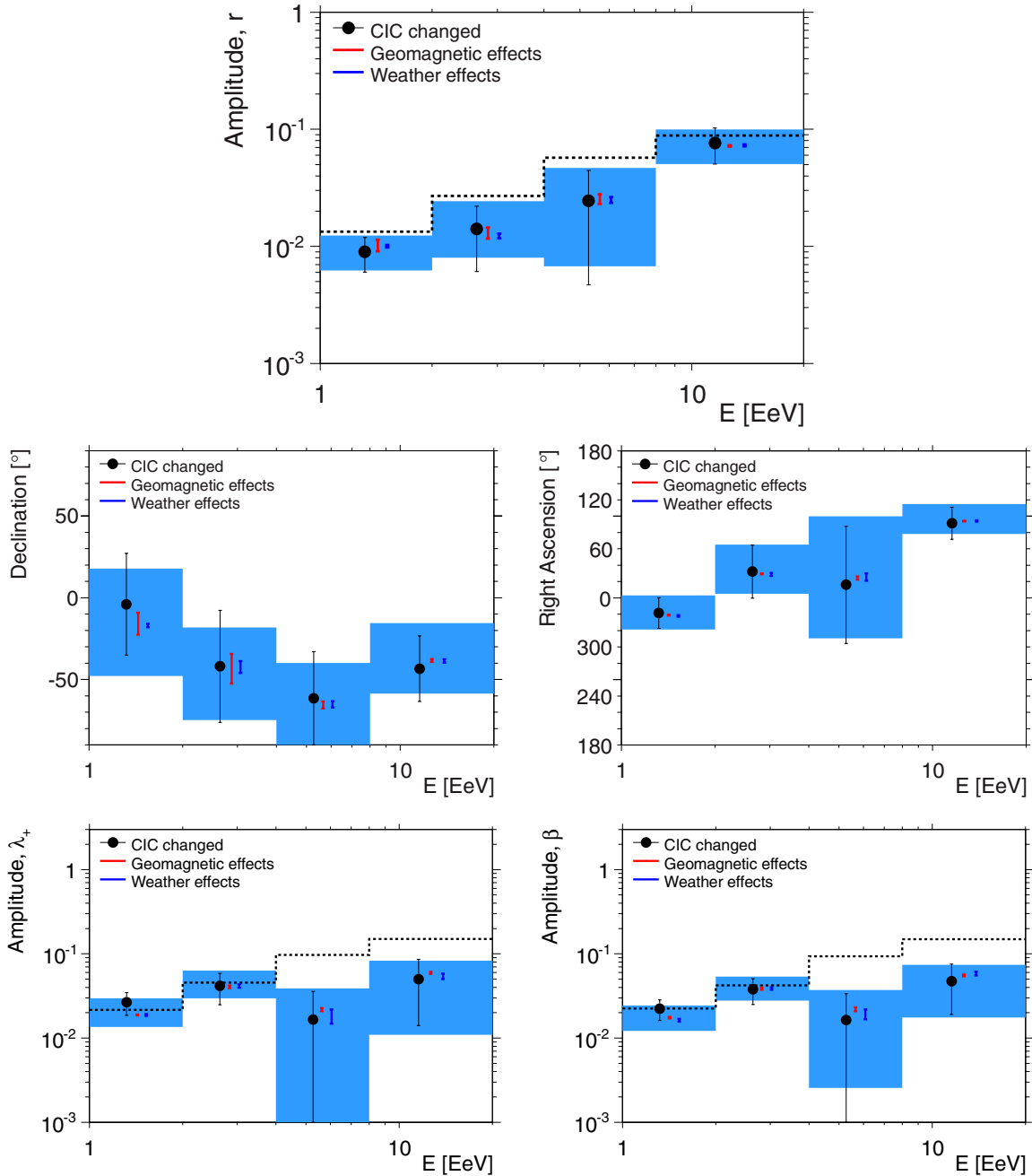
Figure 10. Impact of different sources of systematic uncertainties on the dipole amplitudes (top) and the dipole directions and phases (middle) obtained under the assumption $\ell_{\max} = 1$, and quadrupole amplitudes (bottom) obtained with $\ell_{\max} = 2$, as a function of the energy. The blue bands correspond to the results presented in Figures 5 and 9.

(A color version of this figure is available in the online journal.)

illustrated in the top and middle panels of Figure 10. Meanwhile, both reconstructed quadrupole amplitudes in the energy interval $2 \leqslant E/\text{EeV} \leqslant 4$ are reduced in such a way that they lie now just below the 99% upper bounds for isotropy. Conversely, the amplitudes in the energy interval $1 \leqslant E/\text{EeV} \leqslant 2$ are slightly increased. Below 4 EeV, the determination of the attenuation curve thus appears to bring some systematic uncertainties for determining the quadrupole amplitudes. The two extreme extrapolations performed in this analysis (i.e., b constant with the energy or linearly dependent with the logarithm of the energy) allow us to bracket the possible values.

6.3. Systematic Uncertainties Associated with Corrections for Weather and Geomagnetic Effects

In Section 3, we presented the procedure adopted to account for the changes in shower size due to weather and geomagnetic effects. Since the coefficients α_P, α_ρ, and β_ρ in Equation (1) were extracted from real data, they suffer from statistical uncertainties which may impact in a systematic way the corrections made on $S(1000)$, and consequently may also impact the anisotropy parameters derived from the data set. Besides, the determination of g_1 and g_2 in Equation (2) is based on the
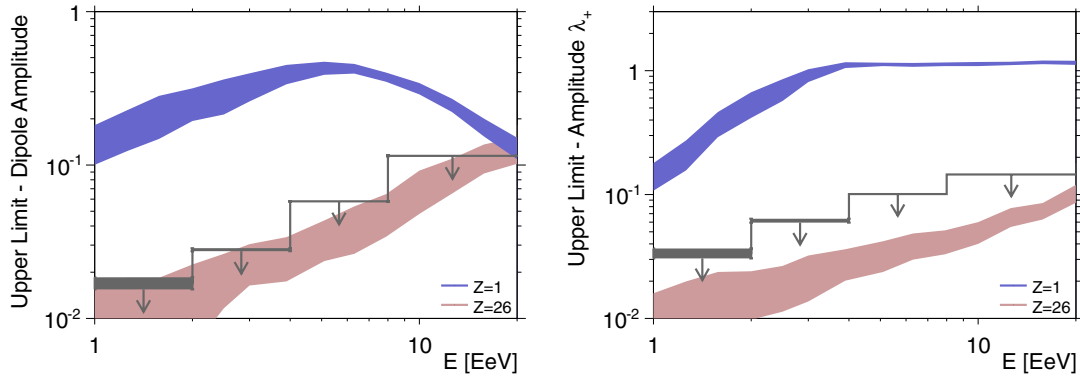
Figure 11. 99% CL upper limits on dipole and quadrupole amplitudes as a function of the energy. Some generic anisotropy expectations from stationary Galactic sources distributed in the disk are also shown for various assumptions on the cosmic-ray composition. The fluctuations of the amplitudes due to the stochastic nature of the turbulent component of the magnetic field are sampled from different simulation data sets and are shown by the bands (see the text).

(A color version of this figure is available in the online journal.)

Table 3
Summary of the Dipolar Analysis ($\ell_{\max} = 1$) Reported in Section 5.2, Together with the Derived 99% CL Upper Limits (UL) on the Amplitudes

ΔE (EeV)	N	$\bar{r}$ (%)	$\bar{\delta}$ (°)	$\bar{\alpha}$ (°)	UL (%)
1–2	360132	1.0 ± 0.4	-15 ± 32	342 ± 20	1.5
2–4	88042	1.6 ± 0.8	-46 ± 28	35 ± 30	2.8
4–8	19794	2.7 ± 2.0	-69 ± 30	25 ± 74	5.8
>8	8364	7.5 ± 2.5	-37 ± 21	96 ± 18	11.4

Table 4
Summary of the Quadrupolar Analysis ($\ell_{\max} = 2$) Reported in Section 5.3, Together with the Derived 99% CL Upper Limits (UL) on the Amplitudes

ΔE (EeV)	$\bar{\lambda}_+$ (%)	$\bar{\beta}$ (%)	UL (λ_+) (%)	UL (β) (%)
1–2	2.0 ± 0.7	1.7 ± 0.6	3.0	2.9
2–4	5.0 ± 1.7	4.2 ± 1.3	6.3	6.1
4–8	1.6 ± 2.0	1.9 ± 1.8	10.0	9.4
>8	4.0 ± 3.4	3.9 ± 2.7	14.5	13.8

simulation of showers. Both the systematic uncertainties associated with the different interaction models and primary masses and the statistical uncertainties related to the procedure used to extract g_1 and g_2 constitute a source of systematic uncertainties on the anisotropy parameters.

To quantify these systematic uncertainties, we repeated the whole chain of analysis on a large number of modified data sets. Each modified data set is built by randomly sampling the coefficients α_P, α_ρ, and β_ρ (or g_1 and g_2 when dealing with geomagnetic effects) according to the corresponding uncertainties and correlations between parameters through the use of a Gaussian probability distribution function. For each new set of correction coefficients, new sets of anisotropy parameters are then obtained. The rms of each resulting distribution for each anisotropy parameter is the systematic uncertainty that we assign. Results are shown in Figure 10, in terms of the dipole and quadrupole amplitudes as a function of the energy. Balanced against the statistical uncertainties in the original analysis (shown by the bands), it is apparent that both sources of systematic uncertainties have a negligible impact on each reconstructed anisotropy amplitude.

7. UPPER LIMITS AND DISCUSSION

From the analyses reported in Section 5, upper limits on dipole and quadrupole amplitudes can be derived at 99% CL (see Appendices C and D). All relevant results are summarized in Tables 3 and 4. The upper limits are also shown in Figure 11 accounting for the systematic uncertainties discussed in the previous section: in the last two energy bins, the upper limits are quite insensitive to the systematic uncertainties because all amplitudes lie well within the background noise.

Below we illustrate the astrophysical interest of these upper limits by calculating the anisotropy amplitudes expected in a toy scenario in which sources of EeV cosmic rays are stationary,

densely and uniformly distributed in the Galactic disk, and emit particles in all directions.

Both the strength and the structure of the magnetic field in the Galaxy, known only approximately, play a crucial role in the propagation of cosmic rays. The field is thought to contain a large-scale regular component and a small-scale turbulent one, both having a local strength of a few microgauss (see, e.g., Beck 2001). While the turbulent component dominates in strength by a factor of a few, the regular component imprints dominant drift motions as soon as the Larmor radius of cosmic rays is larger than the maximal scale of the turbulences (thought to be in the range 10–100 pc). We adopt in the following a recent parameterization of the regular component obtained by fitting model field geometries to Faraday rotation measures of extragalactic radio sources and polarized synchrotron emission (Pshirkov et al. 2011). It consists in two different components: a disk field and a halo field. The disk field is symmetric with respect to the Galactic plane and is described by the widely used logarithmic spiral model with reversal direction of the field in two different arms (the so-called BSS-model). The halo field is anti-symmetric with respect to the Galactic plane and purely toroidal. The detailed parameterization is given in Pshirkov et al. (2011) (with the set of parameters reported in Table 3). In addition to the regular component, a turbulent field is generated according to a Kolmogorov power spectrum and is pre-computed on a three-dimensional grid periodically repeated in space. The size of the grid is taken as 100 pc, so as the maximal scale of turbulences, and the strength of the turbulent component is taken as three times the strength of the regular one.

To describe the propagation of cosmic rays with energies $E \geqslant 1$ EeV in such a magnetic field, the direct integration of trajectories is the most appropriate tool. Performing the forward tracking of particles from Galactic sources and recording those particles which cross the Earth is, however, not feasible within a reasonable computing time. So, to obtain the anisotropy of

cosmic rays emitted from sources uniformly distributed in a disk with a radius of 20 kpc from the Galactic center and with a height of ±100 pc, we adopt a method first proposed in Thielheim & Langhoff (1968) and then widely used in the literature. It consists of back-tracking anti-particles with random directions from the Earth to outside the Galaxy. Each test particle *probes* the total luminosity along the path of propagation from each direction as seen from the Earth. For *stationary sources emitting cosmic rays in all directions*, the flux expected in a given sampled direction is then proportional to the time spent in the source region by the test particles arriving from that direction.

The amplitudes of anisotropy obviously depend on the rigidity E/Z of the cosmic rays, with Z the electric charge of the particles. Since we only aim to illustrate the upper limits, we consider two extreme single primaries: protons and iron nuclei. In the energy range $1 \leqslant E/\text{EeV} \leqslant 20$, it is unlikely that our measurements on the average position in the atmosphere of the shower maximum and the corresponding rms can be reproduced with a single primary (The Pierre Auger Collaboration 2010c). Also, in the scenario explored here and for a single primary, the energy spectrum is expected to reveal a *hardening* in this energy range, whose origin is different from the one expected if the ankle marks the cross-over between Galactic and extragalactic cosmic rays (Linsley 1963) or if it marks the distortion of a proton-dominated extragalactic spectrum due to e^+/e^- pair production of protons with the photons of the cosmic microwave background (Hillas 1967; Blumenthal 1970; Berezinsky et al. 2006, 2004). For a given configuration of the magnetic field, the exact energy at which this hardening occurs depends on the electric charge of the cosmic rays. This is because the average time spent in the source region first decreases as $\simeq E^{-1}$ and then tends to the constant free escape time as a consequence of the direct escape from the Galaxy. The hardening with $\Delta\gamma \simeq 0.6$ observed at 4 EeV in our measurements of the energy spectrum is not compatible with the one expected in this scenario ($\Delta\gamma \simeq 1$). Nevertheless, the calculation of dipole and quadrupole amplitudes for single primaries is useful to probe the allowed contribution of each primary as a function of the energy.

The dipole r and quadrupole λ_+ amplitudes obtained for several energy values covering the range $1 \leqslant E/\text{EeV} \leqslant 20$ are shown in Figure 11. To unambiguously probe amplitudes down to the percent level, it is necessary to generate simulated event sets with $\simeq 5 10^5$ test particles. Such a number of simulated events allows us to shrink statistical uncertainties on amplitudes at the 0.5% level. Meanwhile, there is an intrinsic variance in the model for each anisotropy parameter due to the stochastic nature of the turbulent component of the magnetic field. This variance is estimated through the simulation of 20 sets of $5 10^5$ test particles, where the configuration of the turbulent component is frozen in each set. The rms's of the amplitudes sampled in this way are shown by the bands in Figure 11. While the dipole amplitude steadily increases for iron nuclei, this is no longer the case for protons around the ankle energy. This is because we explore a source region uniformly distributed in the disk. Consequently, the image of the Galactic plane appears less distorted by the magnetic field with increasing energy. This gives rise to an important quadrupolar moment which actually turns out to be the main feature of the anisotropy at large scale.[108]

The dipole and quadrupole λ_+ amplitudes obtained here depend on the model used to describe the galactic magnetic field. We note that recently, a new model was given in Farrar & Jansson (2012), providing improved fits to Faraday rotation measures of extragalactic radio sources and polarized synchrotron emission observations. However, we tested at a few energies that the results obtained are qualitatively in agreement with the ones presented in Figure 11. Similar conclusions were given in Giacinti et al. (2012), where more systematic studies can be found in terms of the field strength and geometry.

Around 1 EeV, there are indications that the cosmic-ray composition includes a significant light component from various measurements of the depth of shower maximum $X_{\max}$ (The Pierre Auger Collaboration 2010c; Abbasi et al. 2010b; Jui et al. 2011). It is apparent that amplitudes derived for protons largely stand above the allowed limits. Consequently, unless the strength of the magnetic field is much higher than in the example used here, the upper limits derived in this analysis exclude the possibility that the light component of cosmic rays comes from Galactic stationary sources densely distributed in the Galactic disk and emitting in all directions. This is in agreement with the absence of any detectable point-like sources above 1 EeV that would be indicative of a flux of neutrons produced by EeV-protons through mainly pion-producing interactions in the source environments (The Pierre Auger Collaboration 2012). On the other hand, if the cosmic-ray composition around 1 EeV results from a mixture containing a large fraction of iron nuclei of Galactic origin, upper limits can still be respected, or alternatively a light component of extragalactic origin would be allowed. Future measurements of composition below 1 EeV will come from the low energy extension HEAT now available at the Pierre Auger Observatory (Mathes et al. 2011). Combining these measurements with large-scale anisotropy ones will then allow us to further understand the origin of cosmic rays at energies less than 4 EeV.

8. SUMMARY

For the first time, a thorough search for large-scale anisotropies as a function of both the declination and the right ascension in the distribution of arrival directions of cosmic rays detected above 1 EeV at the Pierre Auger Observatory has been presented. With respect to the traditional search in right ascension only, this search requires the control of additional systematic effects affecting both the exposure of the sky and the counting rate of events in local angles. All these effects were carefully accounted for and presented in Sections 3 and 4. No significant deviation from isotropy is revealed within the systematic uncertainties, although the consistency in the dipole phases may be indicative of a genuine signal whose amplitude is at the level of the statistical noise. The sensitivity accumulated so far to dipole and quadrupole amplitudes allows us to challenge an origin of cosmic rays from stationary Galactic sources densely distributed in the Galactic disk and emitting predominantly light particles in all directions.

Future work will profit from both the increased statistics and the lower energy threshold that is now available at the Pierre Auger Observatory (Mathes et al. 2011; Sanchez et al. 2011). This will provide further constraints helping to understand the origin of cosmic rays in the energy range $0.1 < E/\text{EeV} < 10$.

---

[108] This feature would remain in the case of a radial distribution of sources following the matter in the Galaxy, though the dipole amplitude would steadily increase above the ankle energy.

APPENDIX A

LARGE-SCALE ANISOTROPIES IN LOCAL COORDINATES

To study the angular distribution in local coordinates for different anisotropic angular distributions $\Phi(\alpha, \delta)$ in celestial coordinates, we restrict ourselves, without loss of generalities, to the case of full detection efficiency ($\epsilon(\theta, \varphi, E) = 1$). Then, the instantaneous arrival direction distribution in local coordinates

reads

$$\frac{d^3 N}{d\theta d\varphi d\alpha^0} \propto \sin\theta \cos\theta \Phi(\theta, \varphi, \alpha^0), \qquad (A1)$$

where $\Phi(\theta, \varphi, \alpha^0)$ is the underlying angular distribution of cosmic rays, expressed in local coordinates. In the case of isotropy, Φ is constant so that once integrated over φ and α^0, the arrival direction distribution is such that $dN/d\sin^2\theta$ is also constant. On the other hand, in case of a dipolar distribution, for instance, Φ is proportional to $1 + r\mathbf{d}(\theta, \varphi, \alpha^0) \cdot \mathbf{n}(\theta, \varphi)$, where $\mathbf{n}$ is a unit vector in local coordinates and $\mathbf{d}$ is the dipole unit vector pointing toward (α_d, δ_d) and expressed in local coordinates by means of Equation (4). To quantify the distortions induced by a dipole in the $dN/d\sin^2\theta$ distribution, we define $\Delta(dN/d\sin^2\theta)$ such that

$$\Delta(dN/d\sin^2\theta) = \frac{1}{r}\left(\frac{dN_{\mathrm{dipole}}/d\sin^2\theta - dN_{\mathrm{iso}}/d\sin^2\theta}{dN_{\mathrm{iso}}/d\sin^2\theta}\right). \qquad (A2)$$

Once multiplied by the dipole amplitude r, $\Delta(dN/d\sin^2\theta)$ directly gives the relative changes in the $dN/d\sin^2\theta$ distribution with respect to isotropy. Carrying out integrations over φ and α^0 yields to

$$\Delta(dN/d\sin^2\theta) = \frac{N_{0,\mathrm{dipole}}}{N_{0,\mathrm{iso}}}\sin\ell_{\mathrm{site}}\sin\delta_d\cos\theta, \qquad (A3)$$

where both intensity normalizations $N_{0,\mathrm{iso}}$ and $N_{0,\mathrm{dipole}}$ are tuned to guarantee the same number of events observed in the covered region of the sky for each underlying angular distribution. This result is shown in the left panel of Figure 12, for the latitude $\ell_{\mathrm{site}} = -35°.2$ of the Pierre Auger Observatory and for different dipole directions. Within the zenithal range $[0°, 55°]$ considered in this article, the relative changes—maximal for $\delta_d = \pm 90°$—amount at most to $\simeq \pm 15\%$. So, even for an amplitude r as large as 10%, the relative changes in $dN/d\sin^2\theta$ would be within $\simeq \pm 1.5\%$, variation which—given the available statistics—is sufficiently low to be considered as negligible. Besides, the same calculation applied to the case of a symmetric quadrupolar anisotropy shows that the variation of $\Delta(dN/d\sin^2\theta)$ is less than $\simeq 0.1\%$, thus being negligible. Consequently, the distribution in $dN/d\sin^2\theta$ can be considered at first order as *insensitive* to large-scale anisotropies, so that any significant deviation from a uniform distribution provides an empirical measurement of the zenithal dependence of the detection efficiency.

It is worth noting that the azimuthal distribution averaged over time is, on the other hand, sensitive to large-scale anisotropies. Repeating the same calculation and integrating now over θ (in this example between 0° and 60°) and α^0 yield the $\Delta(dN/d\varphi)$ relative changes:

$$\Delta(dN/d\varphi) = \frac{N_{0,\mathrm{dipole}}}{N_{0,\mathrm{iso}}}\frac{\sin\delta_d\cos\ell_{\mathrm{site}}}{24}\left(7\tan\ell_{\mathrm{site}} + 3\sqrt{3}\sin\varphi\right). \qquad (A4)$$

This function is shown in the right panel of Figure 12, for $\delta_d = 90°$ (dashed line) and $\delta_d = -90°$ (dotted line). The amplitude of the dipole wave is now $\simeq 0.5$. Also, the influence of a quadrupole on $\Delta(dN/d\varphi)$ is illustrated by the dash-dotted line (oblate symmetric quadrupole in this example). Since, at the Earth latitude of the Pierre Auger Observatory, any genuine large-scale pattern which depends on the declination translates into azimuthal modulations of the event rate *similar* to the
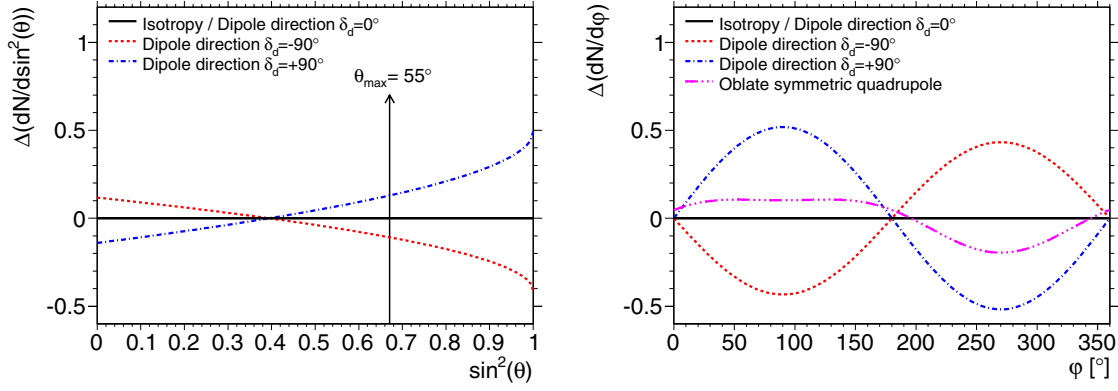
Figure 12. Effect of large-scale anisotropies in local coordinates (left: as a function of $\sin^2\theta$; right: as a function of φ) for an observer located at Earth's latitude $\ell_{site} = -35°.2$ of the Pierre Auger Observatory.

(A color version of this figure is available in the online journal.)

ones induced by experimental effects, it is thus mandatory to accurately model the dependence on azimuth of the detection efficiency for disentangling local from celestial effects.

APPENDIX B

MODULATION OF THE DETECTION EFFICIENCY INDUCED BY A TILTED ARRAY

To estimate the modulation of the detection efficiency induced by a tilted array, we consider here that in the absence of tilt, the corresponding detection efficiency function ϵ_{notilt} depends *only* on the energy and the zenith angle and can be parameterized in a good approximation as

$$\epsilon_{notilt}(E, \theta) = \frac{E^3}{E^3 + E_{0.5}^3(\theta)}, \quad \text{(B1)}$$

where $E_{0.5}(\theta)$ is the zenithal-dependent energy at which $\epsilon_{notilt}(E, \theta) = 0.5$. In case of a tilted array, this parameter depends also on the azimuth angle, which is then the source of the azimuthal modulation of the detection efficiency. To understand this, it is useful to consider for any given shower with parameters (E, θ, φ) the circle in the shower plane corresponding to the region in which a signal S larger than some specified threshold value S_0 is expected. Let $r_0(\zeta)$ denote the radius of this circle, ζ being the tilt angle of the SD array. The detection efficiency, and hence also the parameter $E_{0.5}$, is ultimately a function of the average number of detectors contained in the projection of this circle into the ground, given by

$$\langle n_{det} \rangle (S > S_0) \propto \frac{r_0^2}{h^2 |\mathbf{n}_\perp \cdot \mathbf{n}|}, \quad \text{(B2)}$$

where $h = 1.5$ km is the nominal separation between surface detectors. The radii $r_0(\zeta)$ obtained with the tilted array leading to the same value of $\langle n_{det} \rangle$ can be related to $r_0(\zeta = 0)$ through

$$r_0^2(\zeta) = r_0^2(\zeta = 0)\frac{|\mathbf{n}_\perp \cdot \mathbf{n}|}{\cos\theta}. \quad \text{(B3)}$$

Hence, we can obtain the relation between the energies $E_{0.5}$ with tilt ($E_{0.5}^{tilt}$) and without tilt ($E_{0.5}$) by comparing the cosmic-ray energies required to get the value S_0 at radius $r_0(\zeta)$ and at radius $r_0(\zeta = 0)$. Approximating the lateral distribution function of the signal near the radius r_0 as a power law $S(r) \propto Er^{-3}$, we obtain the following relation:

$$E_{0.5}^{tilt}(\theta, \varphi) = E_{0.5}(\theta)\left(\frac{r_0(\zeta)}{r_0(\zeta = 0)}\right)^3$$
$$\simeq E_{0.5}(\theta)[1 + \zeta \tan\theta \cos(\varphi - \varphi_0)]^3. \quad \text{(B4)}$$

Then, subtracting ϵ_{notilt} from ϵ_{tilt} leads to Equation (9).

APPENDIX C

DETERMINATION OF UPPER LIMITS ON DIPOLE AMPLITUDES

To determine upper limits on the dipole amplitudes, Linsley described the procedure to follow in the case of first harmonic analysis in right ascension (Linsley 1975). Here we adapt this procedure to the case of the dipolar reconstruction adopted in Section 5.2.

Here, the data set is supposed to have been drawn at random from an underlying dipolar distribution characterized by $\mathbf{d}$, whose value is unknown. In the limit of large number of events, the joint p.d.f. $p_{D_X,D_Y,D_Z}(\overline{d}_x, \overline{d}_y, \overline{d}_z)$ can be factorized in terms of three Gaussian distributions $N(\overline{d}_i - d_i, \sigma_i)$:

$$p_{D_X,D_Y,D_Z}(\overline{d}_x, \overline{d}_y, \overline{d}_z; d_x, d_y, d_z)$$
$$= N(\overline{d}_x - d_x, \sigma)N(\overline{d}_y - d_y, \sigma)N(\overline{d}_z - d_z, \sigma_z). \quad \text{(C1)}$$

The joint p.d.f. $p_{R,\Delta,A}(\overline{r}, \overline{\delta}, \overline{\alpha})$ expressing the dipole components in spherical coordinates is then obtained by performing the Jacobian transformation:

$$p_{R,\Delta,A}(\overline{r}, \overline{\delta}, \overline{\alpha}; d, \delta_d, \alpha_d) = \left|\frac{\partial(\overline{d}_x, \overline{d}_y, \overline{d}_z)}{\partial(\overline{r}, \overline{\delta}, \overline{\alpha})}\right| p_{D_X,D_Y,D_Z}$$
$$\times (\overline{d}_x(\overline{r}, \overline{\delta}, \overline{\alpha}), \overline{d}_y(\overline{r}, \overline{\delta}, \overline{\alpha}), \overline{d}_z(\overline{r}, \overline{\delta}, \overline{\alpha}))$$
$$= \frac{\overline{r}^2 \cos\overline{\delta}}{(2\pi)^{3/2}\sigma^2\sigma_z} \exp\left[-\frac{(\overline{r}\sin\overline{\delta} - d\sin\delta_d)^2}{2\sigma_z^2}\right]$$
$$\times \exp\left[-\frac{(\overline{r}\cos\overline{\delta}\cos\overline{\alpha} - d\cos\delta_d\cos\alpha_d)^2}{2\sigma^2}\right]$$
$$\times \exp\left[-\frac{(\overline{r}\cos\overline{\delta}\sin\overline{\alpha} - d\cos\delta_d\sin\alpha_d)^2}{2\sigma^2}\right]. \quad \text{(C2)}$$

Each analyzed data set having been selected at random from an ensemble in which all possible values of $\mathbf{d}$ are equally represented, the various d, δ_d, and α_d combinations have relative probability $p_{R,\Delta,A}(\overline{r}, \overline{\delta}, \overline{\alpha}; d, \delta_d, \alpha_d)/p_{R,\Delta,A}(\overline{r}, \overline{\delta}, \overline{\alpha}; d =$

0). This allows us to define the joint p.d.f. $\tilde{p}_{R,\Delta,A}$ by requiring this ratio to be normalized to unity:

$$
\begin{aligned}
&\tilde{p}_{R,\Delta,A}(\overline{r}, \overline{\delta}, \overline{\alpha}; d, \delta_d, \alpha_d) \\
&= K(r, \delta) \exp\left[\frac{\overline{r}d\cos\overline{\delta}\cos\delta_d\cos(\overline{\alpha}-\alpha_d)}{\sigma^2}\right] \\
&\times \exp\left[\frac{\overline{r}d\sin\overline{\delta}\sin\delta_d}{\sigma_z^2} - \frac{d^2\cos^2\delta_d}{2\sigma^2} - \frac{d^2\sin^2\delta_d}{2\sigma_z^2}\right],
\end{aligned}
\tag{C3}
$$

where the normalization reads

$$
\begin{aligned}
K(r, \delta) &= 2\pi\, I_0\left(\frac{\overline{r}d\cos\overline{\delta}\cos\delta_d}{\sigma^2}\right) \int dd\, d\delta_d \\
&\times \exp\left[-\frac{d^2\cos^2\delta_d}{2\sigma^2} - \frac{d^2\sin^2\delta_d}{2\sigma_z^2} + \frac{\overline{r}d\sin\overline{\delta}\sin\delta_d}{\sigma_z^2}\right].
\end{aligned}
\tag{C4}
$$

I_0 is here the modified Bessel function of the first kind with order 0. Integration of $\tilde{p}_{R,\Delta,A}$ over δ_d and α_d yields the $\tilde{p}_R$ p.d.f. from which upper limits on d can be obtained within a confidence level CL by inverting the relation

$$
\int_{\overline{r}_{\mathrm{data}}}^1 d\overline{r}\, \tilde{p}_R(\overline{r}, \overline{\delta}; d^{\mathrm{UL}}) = \mathrm{CL}
\tag{C5}
$$

Due to the non-uniform directional exposure in declination, the resulting upper limits actually depend on the declination through the dependence of $\tilde{p}_R$ on $\overline{\delta}$. In practice, this dependence is small, which is why we presented in Section 7 upper limits *averaged* over the declination.

APPENDIX D

DETERMINATION OF UPPER LIMITS ON QUADRUPOLE AMPLITUDES

To determine upper limits on quadrupole amplitudes, we rely on Monte Carlo simulations. For each possible amplitude λ_+ (β), we estimate the p.d.f. $p_{\Lambda_+}(\overline{\lambda}_+; \lambda_+)$ ($p_B(\overline{\beta}; \beta)$) with a given number of events N and a given exposure $\tilde{\omega}$. The amplitude λ_+^{UL} such that $\int_{\overline{\lambda}_{+,\mathrm{data}}}^\infty d\overline{\lambda}_+ \tilde{p}_\Lambda(\overline{\lambda}_+; \lambda_+^{\mathrm{UL}}) = \mathrm{CL}$ is a relevant upper limit (and respectively for β^{UL}).

Alternatively to the previous procedure used to derive upper limits on dipole amplitudes, this procedure can lead to upper limits tighter than the upper bounds for isotropy $\overline{\lambda}_{+,99}$ when the measured values of $\overline{\lambda}_{+,\mathrm{data}}$ are smaller than the expected average for isotropy. To cope with this undesired behavior, the upper limits presented in Section 7 are defined as $\max(\overline{\lambda}_{+,99}, \lambda_+^{\mathrm{UL}})$.

REFERENCES

Abbasi, R. U., Abdou, Y., Abu-Zayyad, T., et al. (The IceCube Collaboration) 2010a, ApJ, 718, 194
Abbasi, R. U., Abu-Zayyad, T., Al-Seady, M., et al. (The HiRes Collaboration) 2010b, Phys. Rev. Lett., 104, 161101

Abdo, A. A., Allen, B. T., Aune, T., et al. (The Milagro Collaboration) 2009, ApJ, 698, 2121
Aglietta, M., Alekseenko, V. V., Alessandro, B., et al. (The EAS-TOP Collaboration) 2009, ApJ, 692, L130
Amenomori, M., Ayabe, S., Bi, X. J., et al. (The Tibet AS$_\gamma$ Collaboration) 2006, Science, 314, 439
Beck, R. 2001, Space Sci. Rev., 99, 243
Berezinsky, V. S., Gazizov, A. Z., & Grigorieva, S. I. 2006, Phys. Rev. D, 74, 043005
Berezinsky, V. S., Grigorieva, S. I., & Hnatyk, B. I. 2004, Astropart. Phys., 21, 617625
Billoir, P., & Deligny, O. 2008, J. Cosmol. Astropart. Phys., JCAP02(2008)009
Bird, D. J., Corbató, S. C., Dai, H. Y., et al. (The Fly's Eye Collaboration) 1993, Phys. Rev. Lett., 71, 3401
Blumenthal, G. R. 1970, Phys. Rev. D, 1, 1596
Bonifazi, C. (for the Pierre Auger Collaboration) 2009, Nucl. Phys. B, 190, 20
Bonifazi, C., Letessier-Selvon, A., & Santos, E. M. 2008, Astropart. Phys., 28, 523
Calvez, A., Kusenko, A., & Nagataki, S. 2010, Phys. Rev. Lett., 105, 091101
Candia, J., Mollerach, S., & Roulet, E. 2003, J. Cosmol. Astropart. Phys., JCAP05(2003)003
Compton, A. H., & Getting, I. A. 1935, Phys. Rev., 47, 817
Cutler, D., & Groom, D. 1986, Nature, 322, 434
Eichler, D., & Pohl, M. 2011, ApJ, 742, 114
Engel, R.   (for the Pierre Auger Collaboration) 2007, in Proc. 30th ICRC Mérida, ed. R. Caballero, J. C. D'Olivio, G. Medina-Tanco et al. (Vol. 4; Mexico City: Universidad Nacional Autónoma de México), 385
Farrar, G., & Jansson, R. 2012, ApJ, 757, 14
Giacinti, G., Kachelrie, M., Semikoz, D. V., & Sigl, G. 2012, J. Cosmol. Astropart. Phys., JCAP07(2012)031
Harari, D., Mollerach, S., & Roulet, E. 2010, J. Cosmol. Astropart. Phys., JCAP11(2010)033
Hersil, J., Escobar, I., Scott, D., Clark, G., & Olbert, S. 1961, Phys. Rev. Lett., 6, 22
Hillas, A. M. 1967, Phys. Lett., 24A, 677
Jui, C. C. H. (The Telescope Array Collaboration) 2011, Proceedings of the APS meeting, arXiv:1110.0133
Kachelriess, M., & Serpico, P. 2006, Phys. Lett. B, 640, 225
Lawrence, M. A., Reid, R. J. O., & Watson, A. A. 1991, J. Phys. G: Nucl. Part. Phys., 17, 733
Li, T.-P., & Ma, Y.-Q. 1983, ApJ, 272, 317
Linsley, J. 1963, in Proc. 8th ICRC, ed. R. R. Daniel, P. J. Lavakare, M. G. K. Menon et al. (Vol. 4; Bombay: Tata Inst.), 77
Linsley, J. 1975, Phys. Rev. Lett., 34, 221101
Mathes, H. J. (for the Pierre Auger Collaboration) 2011, in Proc. 32nd ICRC, (Vol. 3; HE 1.4), 149
Nagano, M., Teshima, M., Matsubara, Y., et al. 1992, J. Phys. G: Nucl. Part. Phys., 18, 423
Pesce, R. (for the Pierre Auger Collaboration) 2011, in Proc. 32nd ICRC, Beijing (Vol. 2; HE 1.3), 214
Pshirkov, M. S., Tinyakov, P. G., Kronberg, P. P., & Newton-McGee, K. J. 2011, ApJ, 738, 192
Ptuskin, V., Rogovaya, S. I., Zirakashvili, V. N., et al. 1993, A&A, 268, 726
Sanchez, F. (for the Pierre Auger Collaboration) 2011, in Proc. 32nd ICRC (Vol. 3; HE 1.3), 145
Sommers, P. 2001, Astropart. Phys., 14, 71
The Pierre Auger Collaboration 2004, Nucl. Instrum. Methods A, 523, 50
The Pierre Auger Collaboration 2008, Phys. Rev. Lett., 101, 061101
The Pierre Auger Collaboration 2009, Astropart. Phys., 32, 89
The Pierre Auger Collaboration 2010a, Phys. Lett. B, 685, 239
The Pierre Auger Collaboration 2010b, Nucl. Instrum. Methods A, 613, 29
The Pierre Auger Collaboration 2010c, Phys. Rev. Lett., 104, 091101
The Pierre Auger Collaboration 2011a, Astropart. Phys., 34, 627
The Pierre Auger Collaboration 2011b, J. Cosmol. Astropart. Phys., JCAP11(2011)022
The Pierre Auger Collaboration 2012, ApJ, 760, 48
Thielheim, K. O., & Langhoff, W. 1968, J. Phys. A: Math. Gen., 1, 694
Zirakashvili, V. N., Pochepkin, D. N., Ptuskin, V. S., & Rogovaya, S. I. 1998, Astron. Lett., 24, 139